

Vela Pulsar: Single Pulses Analysis with Machine Learning Techniques

Carlos O. Lousto,^{1,3*} Ryan Missel², Harsh Prajapati³, Valentina Sosa Fiscella^{1,4}, Federico G. López Armengol¹, Prashna Kumar Gyawali², Linwei Wang², Nathan Cahill³, Luciano Combi^{1,4}, Santiago del Palacio⁴, Jorge A. Combi^{4,5}, Guillermo Gancio⁴, Federico García^{4,6}, Eduardo M. Gutiérrez⁴, Fernando Hauscarriaga⁴

¹Center for Computational Relativity and Gravitation, Rochester Institute of Technology, 85 Lomb Memorial Drive, Rochester, New York 14623, USA

²Golisano College of Computing and Information Sciences Rochester Institute of Technology Rochester, NY 14623, USA

³School of Mathematical Sciences, Sciences Rochester Institute of Technology Rochester, NY 14623, USA

⁴Instituto Argentino de Radioastronomía (CCT La Plata, CONICET; CICPBA; UNLP), C.C.5, (1894) Villa Elisa, Buenos Aires, Argentina.

⁵Facultad de Ciencias Astronómicas y Geofísicas, Universidad Nacional de La Plata, Paseo del Bosque, B1900FWA La Plata, Argentina

⁶Kapteyn Astronomical Institute, University of Groningen, P.O. BOX 800, 9700 AV Groningen, The Netherlands

Accepted XXX. Received YYY; in original form ZZZ

ABSTRACT

We study individual pulses of Vela (PSR B0833-45 / J0835-4510) from daily observations of over three hours (around 120,000 pulses per observation), performed simultaneously with the two radio telescopes at the Argentine Institute of Radioastronomy. We select 4 days of observations in January-March 2021 and study their statistical properties with machine learning techniques. We first use density based DBSCAN clustering techniques, associating pulses mainly by amplitudes, and find a correlation between higher amplitudes and earlier arrival times. We also find a weaker (polarization dependent) correlation with the mean width of the pulses. We identify clusters of the so-called mini-giant pulses, with $\sim 10\times$ the average pulse amplitude. We then perform an independent study, with Self-Organizing Maps (SOM) clustering techniques. We use Variational AutoEncoder (VAE) reconstruction of the pulses to separate them clearly from the noise and select one of the days of observation to train VAE and apply it to the rest of the observations. We use SOM to determine 4 clusters of pulses per day per radio telescope and conclude that our main results are robust and self-consistent. These results support models for emitting regions at different heights (separated each by roughly a hundred km) in the pulsar magnetosphere. We also model the pulses amplitude distribution with interstellar scintillation patterns at the inter-pulses time-scale finding a characterizing exponent $n_{ISS} \sim 7 - 10$. In the appendices we discuss independent checks of hardware systematics with the simultaneous use of the two radio telescopes in different one-polarization / two-polarizations configurations. We also provide a detailed analysis of the processes of radio-interferences cleaning and individual pulse folding.

Key words: pulsars: Vela – methods: observational – methods: statistical

1 INTRODUCTION

In 1967, a rapid pulsating radio-source was discovered in the sky (Hewish et al. 1968). This *pulsar* was soon proved to be a rapidly rotating and highly magnetized neutron star (NS) (Pacini 1967; Gold 1968; Goldreich & Julian 1969; Radhakrishnan et al. 1969; Radhakrishnan & Cooke 1969; Sturrock 1971). In the standard model, pulsars have an external magnetic field with a strong dipole moment and, around the magnetic poles of the star, charged particles accelerate and emit a collimated beam of light. The misalignment of the magnetic moment with the rotation axis of the star generates a *light-house* effect that allows us to detect such emission only when the magnetic moment coincides with our line of sight, once every rotational period. Since the first discovery, more than a thousand pulsars have been found (see Lorimer 2008, for a general review).

The radio emission from pulsars is rather weak, varying from a

few μJy to 1 Jy, at 1.4 GHz. For this reason, to obtain a clear profile over the background noise, the observation of pulsars proceeds by integrating over thousands of pulses, with a technique usually called *folding*. This technique is feasible because of the remarkable regularity of the pulses over time. The detection of each individual pulse, however, is achievable for very bright pulsars, and the variability of these single-pulses reveal details of the structure and emission processes in these objects. Particularly, the pulsar of Vela (PSR B0833-45 / J0835-4510), discovered over 50 years ago (Large et al. 1968), has a flux of $S_{1400} = 1.1\text{Jy}$ and has been the focus of many single-pulses studies. The pioneer work of Krishnamohan & Downs (1983) discovered that stronger single-pulses arrive earlier if compared with the mean pulse. Further, to explain deviations of the observed polarization from the dipole model, they proposed that single-pulses are composed of four independent components that originate at different heights in the magnetosphere. Johnston et al. (2001) and Kramer et al. (2002) increased the resolution in time and focused in the variability of the micro-structure, arguing that single-

* E-mail: colsma@rit.edu (COL)

pulses are composed of multiple sweeping beams of light. They also claimed the existence of sporadic giant micro-pulses and a bump in the leading and trailing parts of the profile, respectively, that present a different energy distribution than the rest of the pulse, suggesting a different origin (see also Cairns et al. 2001).

At the same time, the pulsar of Vela is particularly interesting because, being young ($\sim 10^4$ yr), it is prone to have regular *glitches*, sudden speeds up in its rotation frequency ν , with $\Delta\nu/\nu \propto 10^{-9}$, approximately once every three years (Radhakrishnan & Manchester 1969; Reichley & Downs 1969; Dodson et al. 2007). The Vela PSR also manifests several *micro-glitches* over a year (Cordes et al. 1988). These events are thought to be produced by the sudden coupling of a fast rotating superfluid core with the crust of the pulsar, but the details of such coupling have been challenged (Andersson et al. 2012; Chamel 2013; Piekarewicz et al. 2014) and are a matter of current research (see Haskell & Melatos 2015, for a review on models of pulsar glitches). The analysis of single-pulses can bring further insight into the details of the physical mechanism behind these glitches. Remarkably, in 2016, Vela was observed to glitch *live* (Palfreyman et al. 2018). This observation showed that the glitch process took under five seconds, and that the pulsar did not pulse for one period, with the prior pulse to the null being very broad and the two following pulses featuring low linear polarization. The latest glitch (so far) had occurred in 2019, around MJD 58515, and was reported by Sarkissian et al. (2019). The radio timing observations performed at the Argentine Institute of Radioastronomy (IAR) of this event were first summarized in Lopez Armengol et al. (2019) and then expanded in Gancio et al. (2020). A new glitch has just occurred on July 21 2021 (MJD 59417.6) that was first reported in Sosa-Fiscella et al. (2021b).

Given the high rotational frequency of Vela PSR (~ 11 Hz), an observation lasting a few hours involves a large amount of single-pulses ($\sim 10^5$). Even more, a daily observational campaign of these single-pulses represents a challenge to our analysis techniques. The last five years have witnessed a notable increase of the machine learning techniques in the analysis of astrophysical data. In particular, for pulsar data analysis and statistical methods, their main application has been on search and detection of new pulsars in surveys (Lin et al. 2020; Guo et al. 2019; Wang et al. 2019; Morello et al. 2019; Devine et al. 2016; Morello et al. 2014; Zhu et al. 2014). The techniques are also applied to fast radio bursts (FRBs) searches (Zhang et al. 2020) and specialize in extracting pulsars over radio-frequency interference (RFI)/noise (Agarwal et al. 2020; Zhang et al. 2018; Bethapudi & Desai 2018). Also interesting here are the techniques that deal with single pulses (Michilli et al. 2018; Pang et al. 2018). The idea of classifying those individual pulses in terms of amplitude and width, to a first approach, and then in terms of other particular features using machine learning, has already been expressed briefly at the end of Sections 4.3 (in relation to magnetars) and 4.5 (in relation to FRBs) of Gancio et al. (2020). Once we have a robust classification and characterization of families of single pulses, we can study their statistical distributions over different time scales, from a single day, through weeks, or up to years and possibly assess whether there is a connection between the single pulses distribution and the glitching activity.

The use of machine learning algorithms is well suited for the classification of single pulses in at least two ways: Clustering and Supervised learning. In Sec. 3.1 we group pulses with similar features by applying the technique of Density-Based Spatial Clustering of Applications with Noise (DBSCAN) (Schubert et al. 2017), using the criterium of density in data space, setting a threshold and a number of expected clusters, involving an iterative optimization process. In

Table 1. Date of each observation, the corresponding number of single pulses, instantaneous period at the beginning of the observation, and the MJD at the beginning and at the end of each.

Day 2021	initial MJD	final MJD	# pulses	P_{inst} [ms]
Jan. 21	59235.128553	59235.254277	121495	89.407366
Jan. 24	59239.117013	59239.240620	119448	89.407676
Jan. 28	59242.088680	59242.222170	128999	89.407915
Mar. 29	59302.943356	59303.076850	128999	89.413017

Sec. 3.3 we train a Variational AutoEncoder (VAE) method (Kingma & Welling 2014) to reconstruct the observation of the highest signal-to-noise ratio (S/N), and then apply the trained method to the rest of our data. Based on such reconstructions, we apply an algorithm of Self-Organizing Maps (SOM) clustering (Kohonen 1988). In Sec. 3.2 we model the individual pulse amplitude distribution assuming it is due entirely to interstellar scintillation, while in Sec. 3.4 we model the SOM clusters in terms of magnetosphere strata. We close the paper with a discussion in Sec. 4 of future applications of this technique to other bright pulsars that allow single pulse analysis and in particular to Vela close to one of its large glitches.

2 OBSERVATIONS

The main observational program of the Argentine Institute of Radioastronomy consists on the follow up of a set of targeted pulsars, with daily observations of up ~ 3.5 hours. In 2019, the radio telescope Dr. Carlos Varsavsky (A1) was updated to match the same parameters and components as the second radio telescope, Dr. Esteban Bajaja (A2). In this direction, the low noise amplifiers, radio frequency filters, among other components were upgraded. As a result, now both radio telescopes have almost identical front end's and the second polarization of A1 has been recovered, in contrast with the receiver presented in (Gancio et al. 2020). In the case of the very bright pulsar of Vela, IAR's antennas sensitivity allows the detection of single pulses with a time resolution of $73 \mu\text{s}$ (from a 56 MHz sampling averaged over $N_{\text{av}} = 4096$ cycles). The observations used in this paper have been performed simultaneously with A1 and A2. A1 has been set in a single polarization mode that allows for a total 112 MHz bandwidth, while A2 adds its two (circular) polarizations, each with a 56 MHz bandwidth. Both receivers have been chosen to be centered at 1400 MHz and share the same band pass filter (ZX75BP-1280-S+) (see Fig. 3 in Gancio et al. 2020). These different settings have been chosen to see the effects of bandwidth and total power on our analysis as well as the different (local) RFI content of each radio telescope due to their different location (150 meters apart) in the IAR campus.

We analyze six observations on January, 21th, 24th and 28th, 2021, performed with both radio telescopes for over three hours. An additional set of observations was performed on March 29th, 2021, in which we changed the A1 configuration from a single polarization at 112 MHz bandwidth, into the sum of two polarizations of 56 MHz bandwidth each, matching A2 configuration, which remained unchanged. The number of single-pulses in each observation is given in Table 1.

All observations have been cleaned from radio frequency interferences using the code RFIclean (Maan et al. 2021) with protection of the fundamental frequency of Vela (11.184 Hz) at each of the days of observations, as described in the appendix C.

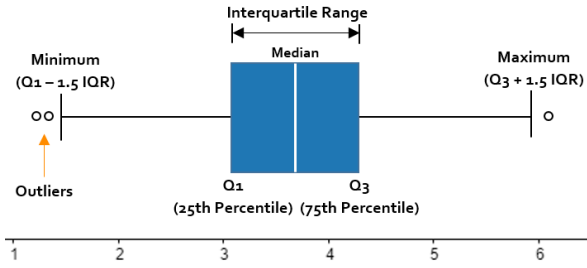


Figure 1. Explanation of the representations in the box plots below.

3 ANALYSIS METHODS

In this section we report the analysis of the observations pulse by pulse via two independent approaches followed by independent teams in a study to compare and interpret results in an unbiased fashion. The large amount of data (120,000 – 130,000 per observation per antenna, totaling nearly a million pulses) is well suited for statistical and machine learning studies. Our first approach has been carried out with DBSCAN, focusing on the peak amplitude, width, and location (time of arrival) of the strongest single-pulses. The second approach has been carried out using a combination of the Variational AutoEncoder reconstruction (VAE) and the self-organizing maps clustering (SOM) techniques. This analysis focuses on a global clustering of the pulses into four main components for which we obtain the mean pulses and its statistical properties. This analysis allow us to identify mini-giant pulses, interstellar scintillation at sub-seconds time-scales, and to model the different emission regions in the pulsar magnetosphere.

In the following subsections we will describe the results of the two approaches for each of the observations in the three days of January 2021, and present March 29th cross-check observations in an appendix D.

3.1 Density based (DBSCAN) techniques and results

We start by characterizing the individual pulses by extracting three basic properties from them: the peak amplitude, the peak position and the width of the peak in time. While we have 1220 bins in time, we focus on a relatively small window (less than 100 bins) where we expect the pulse to arrive, based on the total average pulse. Since the peak in the data looks jagged, we smooth it doing a least squares second order polynomial fit taking five points around the maximum, what provides us with the peak amplitude and peak position. The full width is computed when the pulse arrives to half the maximum amplitude. We also experimented with denoising techniques, but found the above least squares fit was providing more robust results.

We first provide box-plots for the pulses amplitude distributions versus its peak location and versus its width for each of the 8 observations. This follows the nomenclature described in Fig. 1 for its median and 50% around the maximum in blue blocks. Bars in black cover three times this blocks maximum around the 50% width and finally those points lying outside the bars, denoted by circles, are labeled as outliers. The linear box-plots are supplemented by insets with the (log of the) number of pulses in each amplitude slice.

Now that we have extracted and analyzed those three properties of the individual pulses, we feed those as features to the clustering algorithm. As such, each pulse is represented as a three dimensional vector and we can thus classify those points in a 3-dimensional space based on similarities indices. Here we will focus on the Density-Based Spatial Clustering of Applications with Noise (DBSCAN) cluster-

ing method Schubert et al. (2017); Ester et al. (1996) because this algorithm (compared to the classic K-Means) is better at identifying higher density regions and is better at identifying arbitrarily shaped clusters rather than being biased towards spherical clusters. This clustering analysis is an unsupervised learning method that separates the data points into several specific groups, such that the data points in the same group are close in their similarity indices, and data points in different groups have different distance properties. DBSCAN can discover clusters of different shapes and sizes from a large amount of data containing noise and outliers. DBSCAN does not require to specify the number of clusters to use it, but a function is required to calculate the distance between data points and some criteria for the relative scale of distance in that space. For this, we use a default value of 0.6 for the maximum distance between two samples. This is the most important DBSCAN parameter to choose appropriately. Additionally, a minimum number of samples is required for a point to be considered in a neighborhood. Here, we choose 3, including the core point itself, where a core point is one that has at least the minimum number of points required at the maximum distance. Finally, we will consider an Euclidean metric for the distance measures.

DBSCAN has limitations in its performance when inappropriate criterion values and measurements are used, meaning either parameter searches or prior domain knowledge is required to get optimal results. Another limitation is in its ability to generalize to clusters containing highly different densities from the initial ratio of maximum distance to number of points. OPTICS Ankerst et al. (1999) addresses this issue providing a similar clustering at multiple values of the maximum distance with optimized memory usage.

Figure 2 displays the individual pulses of the top amplitude clusters as determined by the DBSCAN clustering algorithm for the 2021-01-28 observation with antenna A2. Those display factors above $\times 10$ the average pulse amplitude and tend to appear earlier than the average. The clustering has different properties of peak amplitude and location, and width to separate them.

In Section 3.3 we will use a different (to Density-based clustering DBSCAN) approach to perform clustering tasks, a hierarchical clustering algorithm based on learned data features, the Self-Organizing Map (SOM).

3.1.1 Observations 2021-01-21

Fig. 3 displays, on the left, the distribution of the pulses amplitudes versus arrival time as measured by the position of their peaks in units of the instantaneous period over 1220 tick marks (see Appendix A). Insets show the histograms of pulse amplitudes for each observation. There is a trend for peaks with larger amplitudes to appear earlier than pulses with lower amplitudes for both radio telescopes observations. On the right column, Fig. 3 displays the distribution of the pulses amplitudes versus its width, measured by the half amplitude of their peaks. There is a trend for peaks with larger amplitudes to appear thinner than pulses with lower amplitude in Radio telescope A1 observations that is not quite confirmed by the corresponding observation with A2, indicating a potential dependence of this effect on the single polarization observations with A1.

We next performed a Density Based Scan analysis of the pulses clustering for each radio telescope’s observation as displayed in Fig. 4, which seems to preferentially select the different clusters by strata of increasing amplitudes with an spread in the peak location and width. It also selects a baseline cluster (in orange, labeled as 0) and an enveloping outlier (in light blue, labeled as -1). We also display the detail of each pulse in the top amplitude DBSCAN clusters over the duration of the observation, labeled by the pulse

2021-01-28 | A2

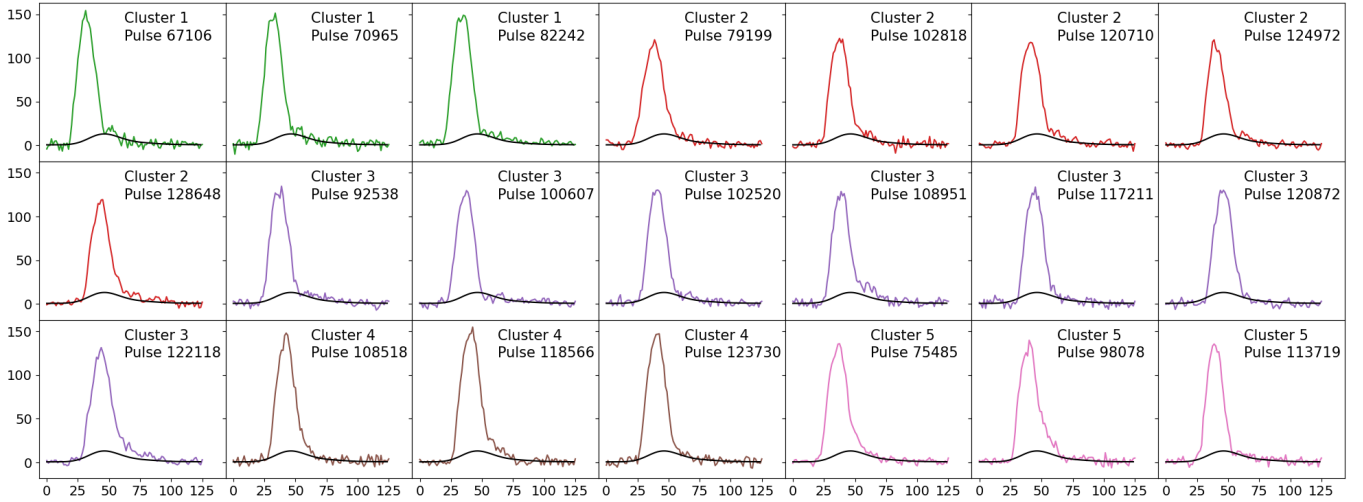


Figure 2. Single pulses in each of the top clusters obtained using DBSCAN. The black line corresponds to the average pulse.

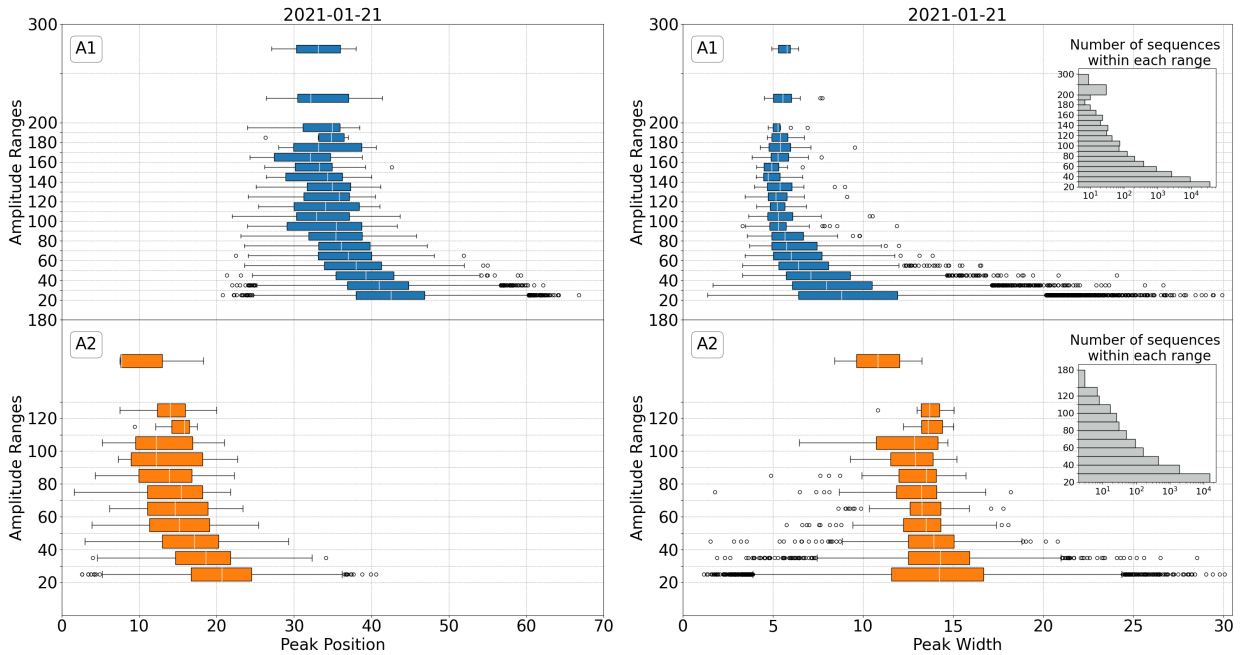


Figure 3. On the left, the distribution of the pulse amplitudes versus arrival time as measured by the position of their peaks for the 2021-01-21 observations. Observations with A1 are on top and with A2 on bottom. On the right, the distribution of the pulses amplitudes versus its mean widths.

index number. There seems to be a preference of large pulses amplitudes towards the second half of the observations from both radio telescopes.

3.1.2 Observations 2021-01-24

Fig. 5 displays the distribution of the pulses amplitudes versus arrival time as measured by the position of their peaks. The insets show the histograms of pulse amplitudes for each observation. We again observe a trend for peaks with larger amplitudes to appear earlier than pulses with lower amplitude in both radio antennas observations indicating that this is a robust feature of the pulses distributions. On

the right column of Fig. 5 we display the distribution of the pulses amplitudes versus its width as measured by the half amplitude of their peaks. The amplitude versus pulse width shows again a preference of narrower high amplitude pulses as seen by the A1 observations, but much less evident in the A2 two polarizations observations, indicating some differences when we observe this features with two polarizations than when we observe them in a single one.

We next performed a Density Based Scan (DBSCAN) analysis of the pulses clustering for each radio telescope's observation as displayed in Fig. 6. This shows the different clusters by increasing amplitudes and some spreading in peak location and width. It also creates a baseline cluster (in orange labeled as 0) and an enveloping

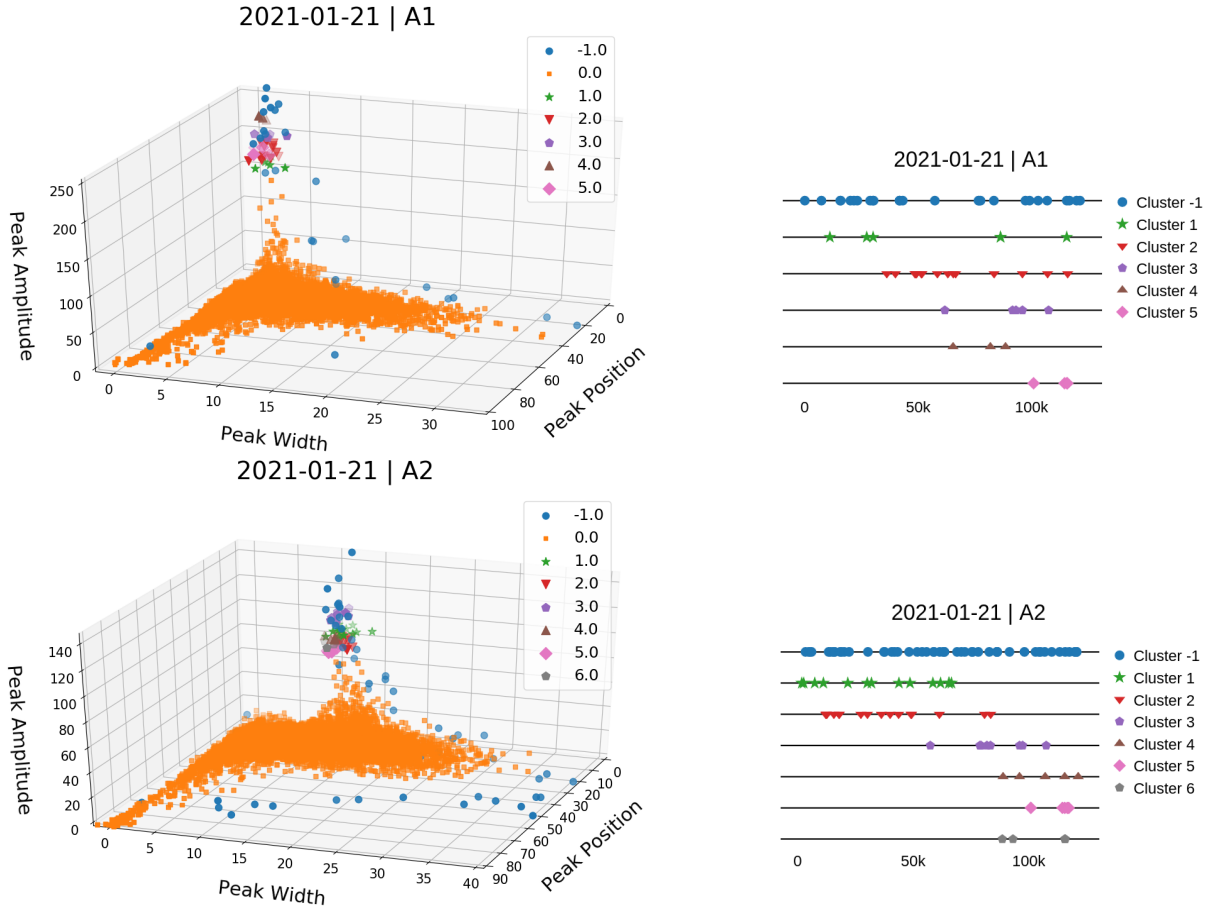


Figure 4. (on the left) 3D distribution of the pulses peak amplitudes, position, and widths for the 2021-01-21 observations. Different colors represent different clusters according to density based scan criteria. (On the right) Distribution of the pulses over the duration of the observations 2021-01-21. Upper figures are for Radio telescope A1, lower figures are for Radio telescope A2 on bottom. Different colors represent different clusters according to DBSCAN criteria.

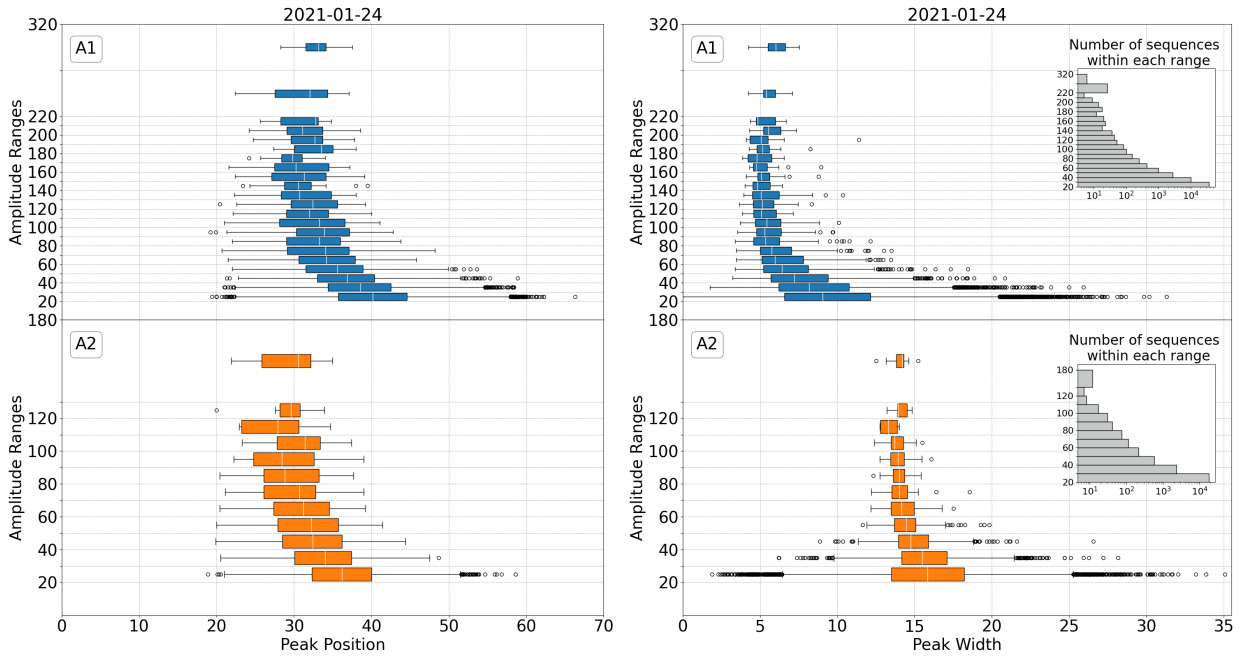


Figure 5. Distribution of the pulses amplitudes versus arrival time as measured by the position of their peaks for the 2021-01-24 observations. On the right the distribution of the pulses amplitudes versus its mean widths for the 2021-01-24 observations. Radio telescope A1 on top and Radio telescope A2 on bottom.

outlier (in light blue, labeled as -1). We also display the detail of each pulse in the top amplitude DBSCAN clusters over the duration of the observation, labeled by the pulse index number. There is a slight preference for the top amplitude pulses to lie in the second part of the observations, but in very small numbers to make a statistically significant trend.

3.1.3 Observations 2021-01-28

The third observation of our selected week at the end of January 2021 is the one with the top S/N according to our analysis in Appendix C. Fig. 7 displays on the left the distribution of the pulses amplitudes versus arrival time as measured by the position of their peaks. Insets show the histograms of pulse amplitudes for each observation. We observe again, that there is a trend for peaks with larger amplitudes to appear earlier than pulses with lower amplitude indicating its a robust feature over time of observation as well as Radio telescope / polarization. We leave the more quantitative study of this feature for the next two sections, where we analyze the effects of scintillation and consider the SOM clustering. On the right, Fig. 7 displays the distribution of the pulses amplitudes versus its mean width as measured by the half amplitude of their peaks. There is again a trend for peaks with larger amplitudes to appear narrower than pulses with lower amplitude in Radio telescope A1 observations that is weakly confirmed by the corresponding observation with Radio telescope A2, suggesting again this effect has a dependence on the single polarization observations with A1. Note also the the magnitude of the amplitudes in the A1 observations nearly doubles that of the A2, again, indicating the higher sensitivity to a wider bandwidth than to the (circular) addition of the two polarizations, although there might be some systematic effects that are better resolved in the two polarization observations, like the width dependence of the pulses on the larger amplitudes.

We performed a DBSCAN analysis of the pulses clustering for each Radio telescope’s observation as displayed in Fig. 8 which selects the different clusters by increasing amplitudes, also creates a baseline cluster (in orange labeled as 0), and an enveloping outlier (in light blue, labeled as -1). We also display the detail of each pulse in the top amplitude DBSCAN clusters over the duration of the observation, labeled by the pulse index number. Those seem to display a preference to appear in the second part of the observation. This seems to indicate perhaps a region of the local sky, towards west, with less interference noise (RFIs), during this week of January 2021.

3.2 Scintillations

Scintillation due to the interstellar media can change the intensity of the pulses. Fig. 9 shows a histogram of the projected pulse S/N for A1 and A2. The line shows the estimated probability density function (PDF) from scintillation (Cordes & Chernoff 1997),

$$f_S(S|m_{\text{ISS}}) = \frac{(S m_{\text{ISS}}/S_0)^{m_{\text{ISS}}}}{S \Gamma(m_{\text{ISS}})} \exp\left(\frac{-S m_{\text{ISS}}}{S_0}\right) \Theta(S), \quad (1)$$

where m_{ISS} is the number of scintles, S_0 is the mean value of the signal S (i.e., $S_0 = \langle S/N \rangle$), and Θ is the Heaviside step function. Since $S \propto T_{\text{peak}}$ (Lorimer & Kramer 2012), it follows that T_{peak} also obeys the PDF in Eq. (1). Here we will explore the possibility of modeling the individual pulses amplitude distribution entirely in terms of a pure interstellar scintillation effect. We therefore calculate m_{ISS} by fitting the observed single pulse peak amplitudes for each Radio telescope. The bin size is determined using the Knuth’s rule (Knuth 2006) algorithm provided in `astropy` (Astropy Collaboration

Table 2. Adjusted values of m_{ISS} for each set of observations and the Jensen-Shannon divergence test D_{JS} -value for each fitting. * Was performed in two polarizations at half the bandwidth

	Date	m_{ISS}	S_0	D_{JS}
A1	Jan 21	7.38 ± 0.11	18.735 ± 0.068	0.117
	Jan 24	7.378 ± 0.112	19.169 ± 0.07	0.121
	Jan 28	6.597 ± 0.118	20.057 ± 0.092	0.125
	*Mar 29	8.186 ± 0.073	7.065 ± 0.014	0.119
A2	Jan 21	10.012 ± 0.091	14.389 ± 0.026	0.099
	Jan 24	9.911 ± 0.098	14.9 ± 0.03	0.104
	Jan 28	9.024 ± 0.103	17.482 ± 0.043	0.11
	Mar 29	9.756 ± 0.093	15.418 ± 0.03	0.106

et al. 2013, 2018). We also normalize the number of observations in each bin by the total number of single pulses in each observation. For each of these fittings we perform a Jensen-Shannon divergence test (Mateos et al. 2017) to quantify the difference between the empirical and the theoretical distribution. Table 2 gives the scintillation fit parameters of the amplitude versus the number of pulses (the insets in Figs. 3,5,7,D2) for the four days of observation on both radio telescopes.

As a result, for Vela, we find $m_{\text{ISS}} \sim 6.6 - 7.4$ with A1 and $m_{\text{ISS}} \sim 9 - 10$ for A2. In contrast, in Sosa Fiscella et al. (2021a), for J0437–4715, we obtained $m_{\text{ISS}} = 2.67 \pm 0.31$ for A1 and $m_{\text{ISS}} = 2.17 \pm 0.25$ for A2 when using 217 minutes-long observations. We also note the large value of the m_{ISS} found in comparison to the typical $m_{\text{ISS}} < 2$ found for longer time scales and different radio-frequencies. Cordes (2000) found two scintillation scales observing Vela at 2.5 GHz of 15s and 26s. Rescaling those scales to our observing frequency, 1400 MHz, we find time scales of $\Delta t_{d,1} = 7.48$ s and $\Delta t_{d,2} = 12.97$ s. Likewise we rescale the scintillation bandwidths to 1400 MHz, and find $\Delta \nu_{d,1} = 3.84$ MHz and $\Delta \nu_{d,2} = 6.49$ MHz, respectively. We can now compare our values of m_{ISS} with theoretical estimations via the formula (Cordes & Chernoff 1997)

$$m_{\text{ISS}} \approx \left(1 + \eta_t \frac{T}{\Delta t_d}\right) \left(1 + \eta_\nu \frac{BW}{\Delta \nu_d}\right) \quad (2)$$

where η_t and η_ν are filling factors ~ 0.25 . The estimated m_{ISS} for $T = 0.089$ s A1 ($BW = 112$ MHz) and for A2 ($BW = 56$ MHz) are $m_{\text{ISS},1} = 8.3$ and $m_{\text{ISS},1} = 4.7$ for A1 and A2 respectively, and $m_{\text{ISS},2} = 5.3$ for A1 and $m_{\text{ISS},2} = 3.2$ for A2.

We then conclude that m_{ISS} over a shorter (0.089 seconds) timescale is expected to be smaller than measured for A2 and polarization dependent (values roughly match the one-polarization measures of A1). We also find a relatively good agreement between the observational data and the theoretical PDF, showing that Eq. (1) holds valid even at such short timescales. Nonetheless, we also note an excess in the number of high-amplitude single pulses that cannot be explained solely on the basis of scintillation. Those represent several thousands of pulses, and leave room for the interpretation in terms of the mini-giant pulses discussed in the previous Sec. 3.1. Besides, the Jensen-Shannon divergence test D_{JS} values displayed in Table 2 are closer to zero than to one (the ideal fit). This opens the possibility of a different sort of modeling to the pulse amplitude distribution, requiring a complementary approach to the one provided above that we will describe next.

3.3 Self-Organizing Map (SOM) techniques and results

This section describes a deep neural network-based machine learning method for unsupervised clustering of the individual pulses of

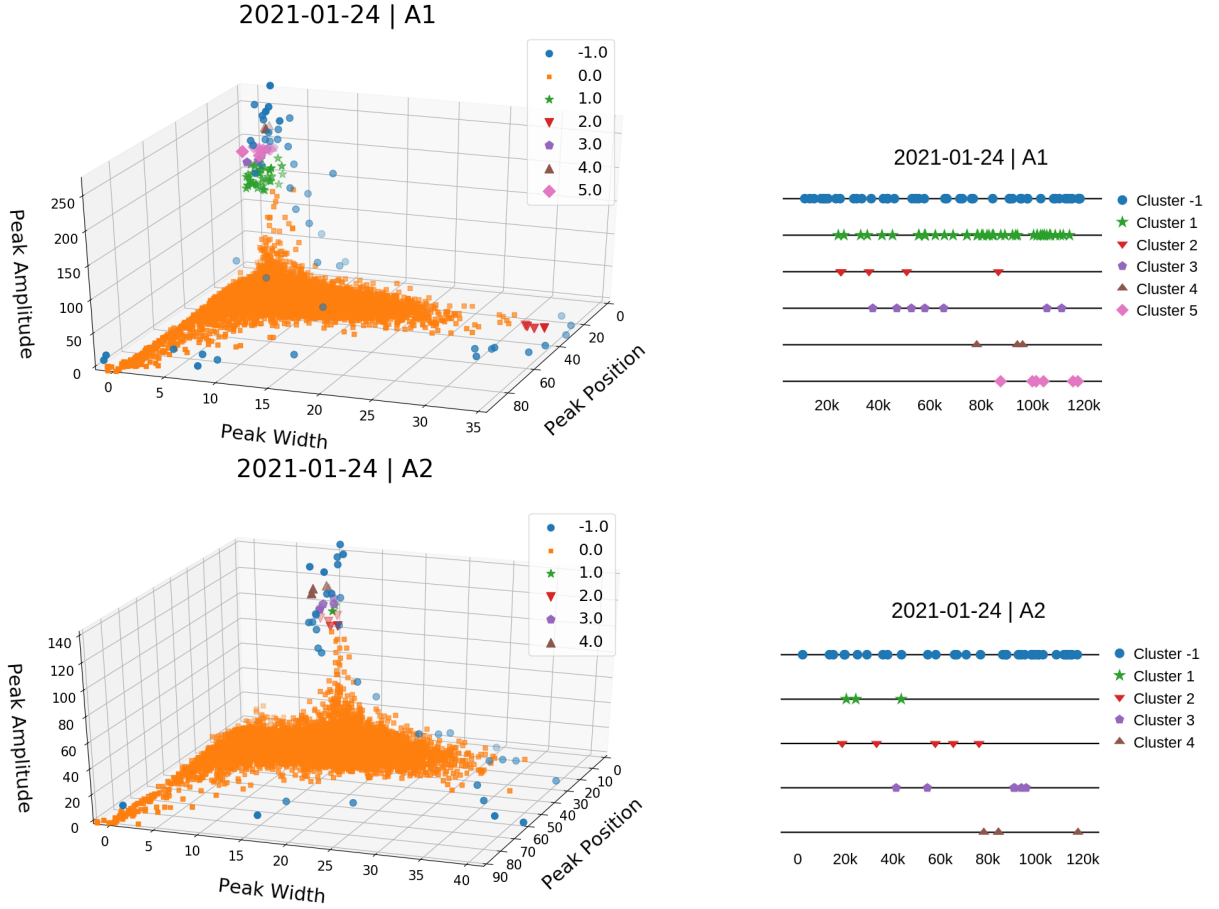


Figure 6. (On the left) 3D distribution of the pulses peak amplitudes, position, and widths for the 2021-01-24 observations. Different colors represent different clusters according to density based scan criteria. (On the right) Distribution of the pulses over the duration of the observations 2021-1-24. Upper figures as for Radio telescope A1, lower figures are for Radio telescope A2 on bottom. Different colors represent different clusters according to DBSCAN criteria.

Vela. In recent years, deep learning has produced remarkable results across many domains, including computer vision, natural languages, and medical imaging (LeCun et al. 2015). With deep learning, one tries to learn representations of the data hierarchically (hence the term deep). The underlying representations capture variations of the data explaining different attributes of the data. Often these representations are regressed to the target prediction because of the interest in the prediction model. In our case, we are more interested in the underlying attributes themselves and resort to unsupervised learning. As we show later, these representations can be grouped into different meaningful clusters of the individual pulses.

In deep learning literature, there are various unsupervised approaches to learn or capture the representations of the data. The most common ones include the autoencoder and its variants, a class of deep learning algorithms that take in the input and try to reconstruct the same input by passing it through the low-dimensional bottleneck subjected to different regularizations (e.g., sparsity). In our case, we consider a variational autoencoder (VAE) which is a probabilistic model with stochastic latent space (Kingma & Welling 2014). Formally, given an individual pulse \mathbf{x}_i , we estimate the mean μ and standard deviation σ using a deep encoder. We then sample a latent vector \mathbf{z}_i from the approximated Gaussian distribution $q_\phi(\mathbf{z}_i|\mathbf{x}_i)$ and pass it to the deep decoder to reconstruct the original signal $p_\theta(\mathbf{x}_i|\mathbf{z}_i)$. The whole model is trained together using evidence lower

bound objective:

$$\log p(\mathbf{x}) \geq \mathcal{L} = \mathbb{E}_{q_\phi(\mathbf{y}|\mathbf{x})} [\log p_\theta(\mathbf{x}|\mathbf{y})] - KL(q_\phi(\mathbf{y}|\mathbf{x})||p(\mathbf{y})) \quad (3)$$

The first term can be represented as the data reconstruction objective and metrics such as the mean squared error or negative log-likelihood as standard choices (Kingma & Welling 2014). The second penalty term constrains the approximated posterior distribution of our latent variable \mathbf{z} to be similar to a given prior $p(\mathbf{z})$ by minimizing the Kullback-Leibler divergence. For the prior $p(\mathbf{z})$, we consider isotropic Gaussian distribution, a standard option in VAE models. We explored other priors as well, which we discuss in Appendix B.

After training the VAE, we consider the Self-Organizing Map (SOM) for unsupervised clustering. SOM is a type of neural network that produces a low-dimensional map (2D), a discretized representation of the input samples. In a typical SOM (Kohonen 1988) with a total of M nodes, $\mathcal{V} = \{v_1, v_2, \dots, v_M\}$, on a two-dimensional grid, we learn a so-called weight vector \mathbf{r}^v for each node $v \in \mathcal{V}$ such as to minimize the distance between each input data and its distance to the closest weight vector (also known as the Best Matching Unit (BMU)). During training, these node weight vectors are updated towards the input data without destroying the topological structure. This is done by dragging neighboring nodes alongside the node being updated. Once trained, the weight vectors on the SOM nodes provide prototypes of the input data, where similar data will be mapped to neighboring prototypes. The SOM can be seen as a generalized case

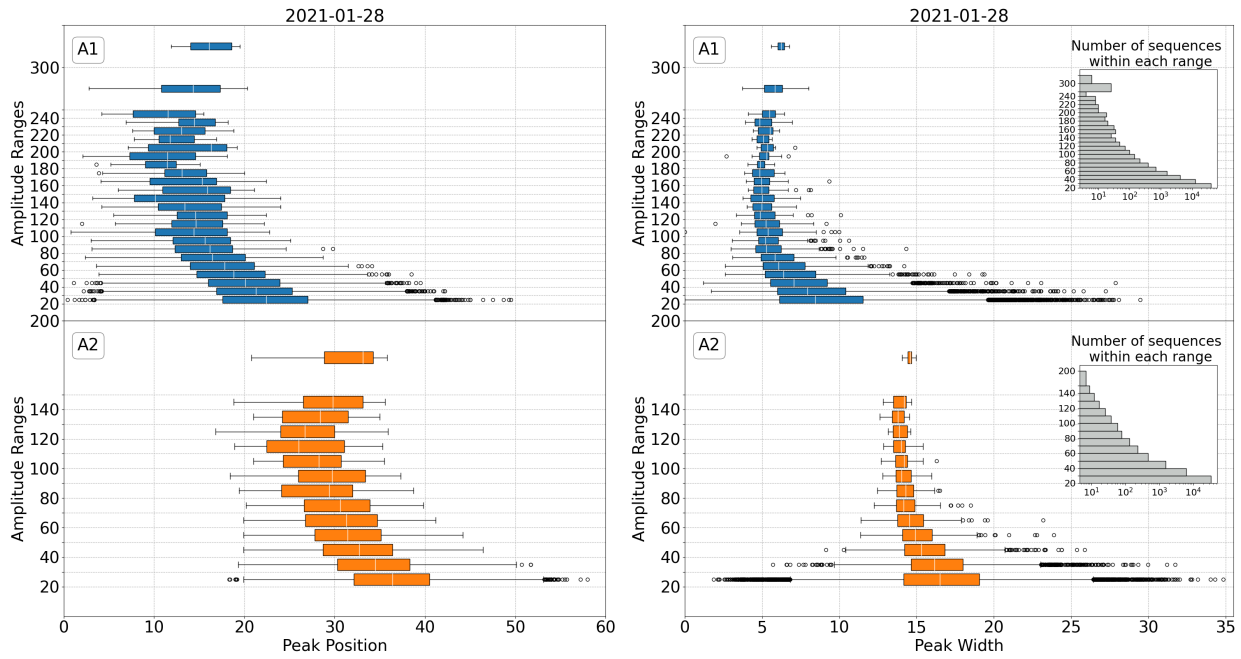


Figure 7. Distribution of the pulses amplitudes versus arrival time as measured by the position of their peaks for the 2021-01-28 observations. Distribution of the pulses amplitudes versus its mean widths for the 2021-01-28 observations. Radio telescope A1 on top and Radio telescope A2 on bottom. The differences in behavior can be attributed to the single polarization (A1) versus two polarizations (A2) observations.

of the K-Means algorithm, where K-Means represents a subclass where the nodes exert no influence on each other during updates.

We consider both the latent representation of the signal and the original signal as the input data to the SOM algorithm. Since the original signal is noisy, we consider reconstructed signal $\hat{\mathbf{x}}_i \sim p_\theta(\mathbf{x}_i|\mathbf{z}_i)$ (some samples are provided in Fig. 10) as the input to the SOM, given that they offer a noiseless approximation of the original signal \mathbf{x}_i . We present the schematic diagram of VAE and usage of SOM for clustering in Fig. 11.

In Fig. 10 we display representative original and VAE reconstructed pulses of each of the SOM clusters for the observation of the 2021-01-28 for each antenna. This data has been later used to train the VAE reconstruction on all other days of observation. This process shown robustness and close agreement with the untrained reconstruction of individual days of observation.

3.3.1 Observations 2021-01-21

In Fig. 12 we display the average value of the pulses in each SOM cluster for each Radio telescope observation. Those have been obtained by first applying a reconstruction of the raw pulses with the VAE technique, for which we have used the reconstruction of our best day of observation (according to the analysis in Appendix C) as a training case to apply to the rest of the days of observation. This training has been applied for each antenna individually. SOM allows us to specify then the number of clusters we seek to subdivide the whole set. We have studied several possible cases, 4, 6, 10, 25, 100, finding that the simplest four cluster analysis presents the most robust results. In fact we observe in Fig. 12 the similarity of the mean clustering between the two antennas observations (we also studied average vs. centroid's clusters). While the total number of members of each cluster changes, the qualitative mean value of the pulses (average pulse over the entire cluster) seems to be robust. We also note the visual displacement towards earlier times of the center and peak

of each cluster average pulse for those with the largest amplitude with respect to each other and with respect to the total average pulse, in the plot denoted by the black dashed curve and labeled as 0. This would be the usual reference pulse we would obtain from the total observation. We also see that largest cluster (labeled as 1), counting a few hundred pulses, is a factor about 5 larger in amplitude for than the average pulse. Both features in qualitative agreement with the statistical analysis of the previous Sec. 3.1.

Table 3 give a quantitative account of the results displayed in Fig. 12. For each antenna's observation we provide the number of pulses of each cluster # pulses; peak location from the index of the maximum value in the pulse sequence; peak height from the maximum value of the pulse sequence; peak width done by first finding the maximum value of the sequence, then performing full-width half maximum of peak (library used for this: https://docs.scipy.org/doc/scipy/reference/generated/scipy.signal.peak_widths.html); for the peak skew we evaluated the Fisher-Pearson coefficient of skewness (using the scipy for this computation <https://docs.scipy.org/doc/scipy/reference/generated/scipy.stats.skew.html>). The trend in the peak location towards later times is clear and above the quoted errors in its determination. Note that the cluster 4, the most numerous, is (necessarily) showing a later arrival than the average total pulse, labeled as 0. A trend is also marginally seen in the width of the pulse, with narrower values for the higher amplitude clusters while also carrying a higher skewness. Although specific numbers differ in both antennas observations, the trends seem to be the same.

3.3.2 Observations 2021-01-24

In Fig. 13 we display the average value of the pulses in each SOM cluster for each Radio telescope observation. Those have been obtained by first applying a reconstruction of the raw pulses with the VAE technique, for which we have used the reconstruction of our

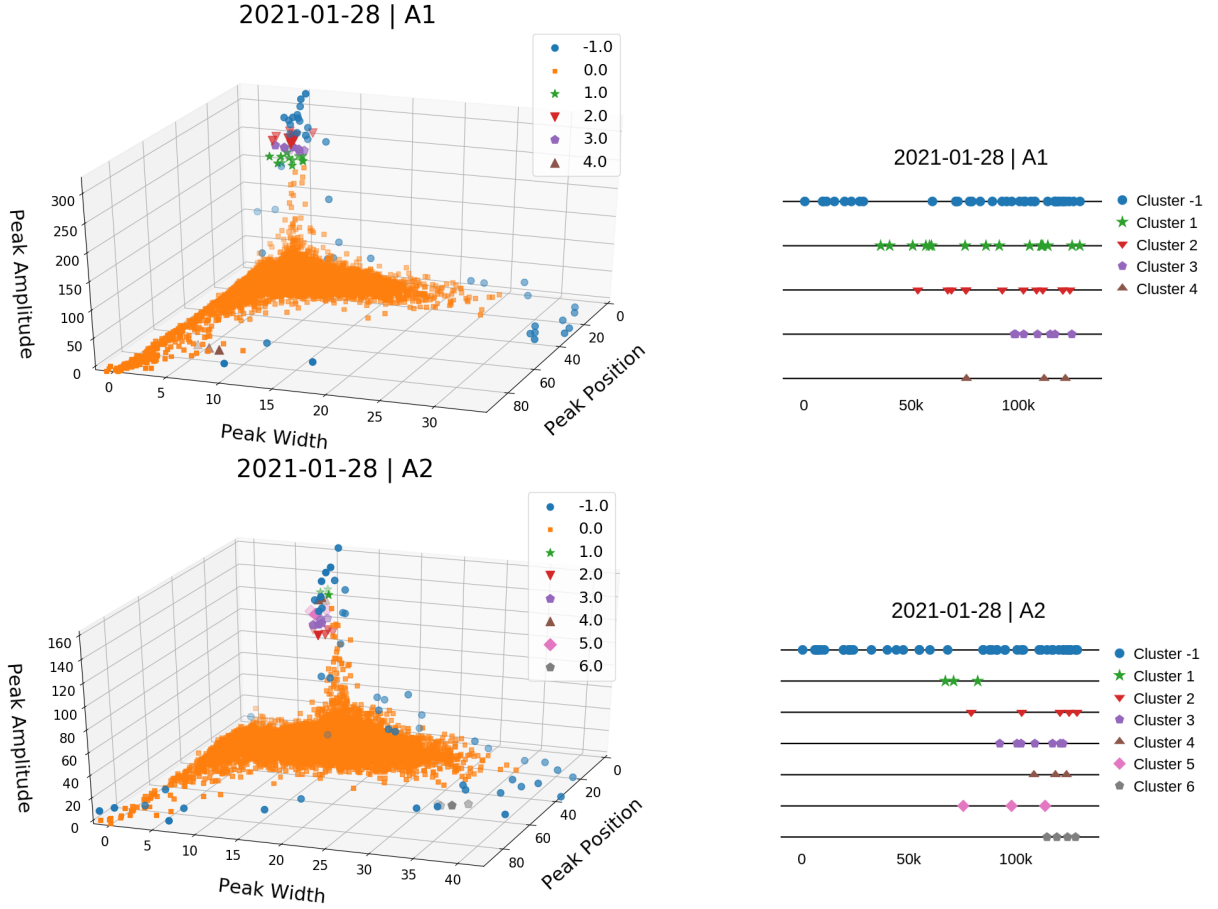


Figure 8. (On the left) 3D distribution of the pulses peak amplitudes, position, and widths for the 2021-01-28 observations. Different colors represent different clusters according to density based scan criteria. (On the right) Distribution of the pulses over the duration of the observations 2021-01-28. Upper figures are for Radio telescope A1, lower figures are for Radio telescope A2 on bottom. Different colors represent different clusters according to DBSCAN criteria.

Table 3. SOM Clustering for 2021-01-21 observations with Antennas 1 and 2.

	Cluster #	0	1	2	3	4
A1	# pulses	121495	244	2203	18138	100910
	peak loc	99.28 ± 5.70	84.99 ± 1.89	87.75 ± 2.15	93.28 ± 3.13	100.64 ± 5.05
	peak height	16.64 ± 10.40	95.24 ± 49.60	36.47 ± 22.83	24.70 ± 14.26	14.57 ± 6.07
	peak width	17.76 ± 4.53	6.05 ± 1.13	9.73 ± 3.00	11.70 ± 3.32	18.74 ± 4.00
	peak skew	2.49 ± 0.42	4.68 ± 0.53	3.51 ± 0.56	2.90 ± 0.41	2.38 ± 0.31
	Cluster #	0	1	2	3	4
A2	# pulses	121495	349	11262	21502	88382
	peak loc	100.31 ± 4.81	87.75 ± 2.84	93.55 ± 3.25	95.30 ± 2.78	102.44 ± 3.38
	peak height	12.40 ± 6.16	64.91 ± 23.05	23.17 ± 7.25	13.90 ± 2.91	10.45 ± 3.37
	peak width	17.44 ± 1.25	14.52 ± 0.55	17.51 ± 1.00	21.58 ± 0.97	23.53 ± 1.83
	peak skew	2.09 ± 0.22	2.98 ± 0.10	2.46 ± 0.13	2.17 ± 0.13	2.01 ± 0.18
	Cluster #	0	1	2	3	4

best day of observation (according to the analysis in Appendix C) as a training case to apply to the rest of the days of observation. This training has been applied for each antenna individually. SOM allows us to specify then the number of clusters we seek to subdivide the whole set. We have studied several possible cases, 4, 6, 10, 25, 100, finding that the simplest four cluster choice represents the most robust results. We observe again in Fig. 13 the similarity of the mean clustering between the two antennas observations. While the total number of members of each cluster changes, the qualitative mean value of the pulses (average pulse over the entire cluster) seems to be robust. We also note the visual displacement towards earlier times

of the center and peak of each cluster average pulse for those with the largest amplitude with respect to each other and with respect to the total average pulse, in the plot denoted by the black dashed curve and labeled as 0. This is the usual reference pulse we obtain from the total observation. We also see that the largest amplitude cluster (labeled as 1), counting a few hundred pulses, is a factor about 5 larger in amplitude than the average pulse. Both features are in qualitative agreement with the statistical analysis of the previous section 3.1. Another interesting feature of the average pulses for each cluster is particularly evident in the A2 observations: The right shoulder of the pulses superpose (this is also evident in the Jan. 21 observations),

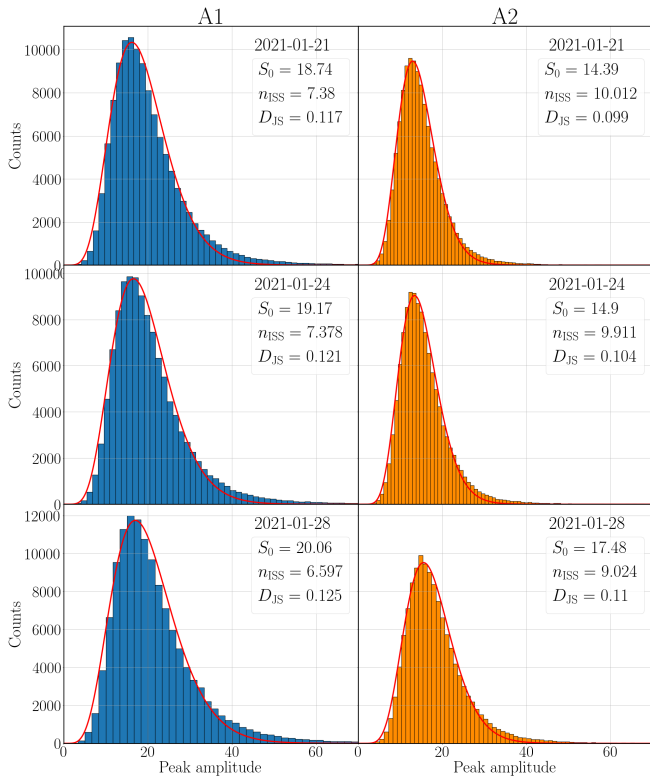


Figure 9. Histograms of projected pulse amplitude for J0835–4510 for A1 (left column) and A2 (right column) for the January 2021 observations. The line shows the estimated scintillation distribution from fitting n_{ISS} in Eq. (1).

indicating a sort of superposition of components at earlier arrival times.

Table 4 give a quantitative account of the results displayed in Fig. 13. For each antenna’s observation on 2021-01-24, we provide the number of pulses of each cluster # pulses; peak location from the index of the maximum value in the pulse sequence; peak height from the maximum value of the pulse sequence; peak width done by first finding the maximum value of the sequence, then performing full-width half maximum of peak; for the peak skew we evaluated the Fisher-Pearson coefficient of skewness. The trend in the peak location towards later times is clear and above the quoted errors in its determination. Note that the cluster 4, the most numerous, is (necessarily) showing a later arrival than the average total pulse, labeled as 0. A trend is also marginally seen in the width of the pulse, with narrower values for the higher amplitude clusters while also carrying a higher skewness. Although specific numbers differ in both antennas observations, the trends seem to be the same.

3.3.3 Observations 2021-01-28

In Fig. 14 we display the average value of the pulses in each of the four SOM cluster for each Radio telescope observation. Those have been obtained by first applying a reconstruction of the raw pulses with the VAE technique. Accordingly to the analysis in Appendix C this observations of the 2021-01-28 are the best regarding its signal-to-noise ratio and are the ones used (for each antenna) for VAE pulse reconstruction training for the rest of the observing days. We observe again in Fig. 14 the similarity of the mean clustering between the two antennas observations. While the total number of

members of each cluster changes, the qualitative mean value of the pulses (average pulse over the cluster) seems to be robust. We also note again the visual displacement towards earlier times of the center and peak of each cluster average pulse with the largest amplitude with respect to each other and with respect to the total average pulse. Most notably here is the amplification factor of the cluster 1 with respect to the total average pulse nearing a factor ten, although being less numerous than during previous observations days. Note also that in the A2 observations there seems to be a superposition of the cluster pulses profile at late times. This feature is also true in the previous two days of observations (and the March observation displayed in the Appendix D3 in A2, clearly displaying the earlier arrival of the higher amplitude components.

Table 5 gives a quantitative account of the results displayed in Fig. 13. For each antenna’s observation on 2021-01-28, we provide the number of pulses of each cluster # pulses; peak location from the index of the maximum value in the pulse sequence; peak height from the maximum value of the pulse sequence; peak width done by first finding the maximum value of the sequence, then performing full-width half maximum of peak; for the peak skew we evaluated the Fisher-Pearson coefficient of skewness. We observe again that the trend in the peak location towards later times is clear and above the quoted errors in its determination. Note that the cluster 4, the most numerous, is (necessarily) showing a later arrival than the average total pulse, labeled as 0. A trend is also marginally seen in the width of the pulse, with narrower values for the higher amplitude clusters while also carrying a higher skewness. Although specific numbers differ in both antennas observations, the trends seem to be the same showing the robustness of the effect.

In the next section we will provide a simple geometrical interpretation of these four components and its properties, in particular the appearance of the earlier high amplitude pulses and its relatively narrower properties, particularly in one polarization.

3.4 Geometrical modeling of the cluster components

As presented Sec. 3.2, the excess of high amplitude pulses cannot be explained solely due to effects of scintillation. In Sec. 3.3 we also find that each cluster has a different average peak location, with brighter pulses arriving earlier. Therefore, following the classic work of Krishnamohan & Downs (1983), we may attribute these variations in pulse amplitude and location to different altitudes in the neutron star magnetosphere where the pulses of each cluster are emitted. To this end, we measure the displacement of each cluster peak location relative to the average pulse location, and then relate those pulse displacements to differences in the emission altitude by

$$h - \bar{h} = \frac{x - \bar{x}}{n_{\text{bins}}} cP, \quad (4)$$

where x and h are the cluster peak location and altitude in the magnetosphere, \bar{x} and \bar{h} are the average peak location and the average altitude (corresponding to cluster 0), n_{bins} is the number of time bins in each pulse (in our case, 1220), and P is the pulsar rotational period. Fig. 15 displays the results of applying this model to each of the four days of observation for each antenna. The right hand side ordinate gives the components distances to the average pulse reference height in the pulsar magnetosphere. We note the consistency between the components for each of the four days and for each individual antenna’s observations. The four components appear to be almost equidistant (this maybe an effect of the SOM clustering method) and roughly of the order of ~ 100 kilometers.

More quantitative results are presented in Table. 6. Cluster 4,

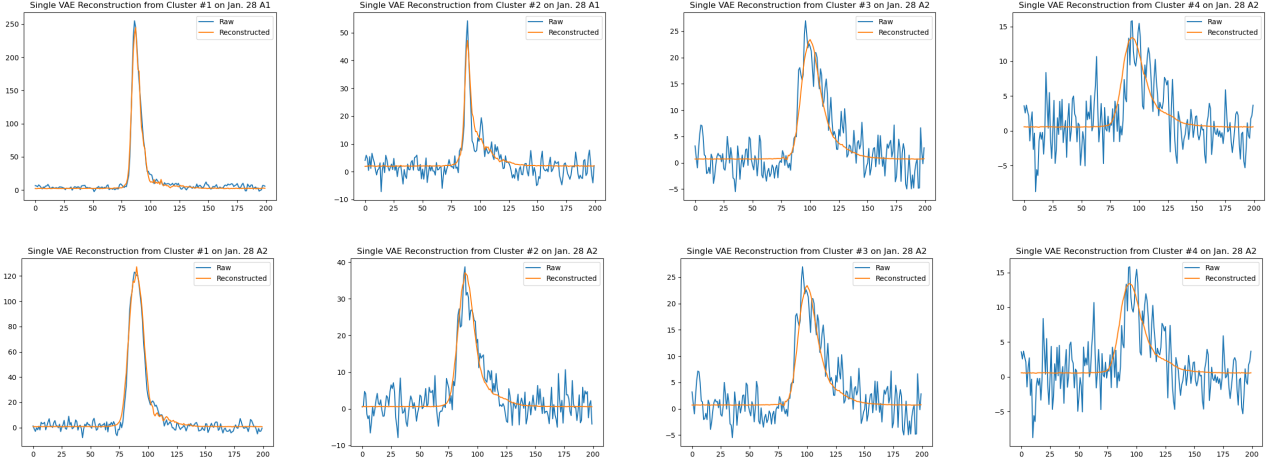


Figure 10. Representative VAE reconstruction individual signals for the observations 2021-01-28 from each of the four SOM clusters.

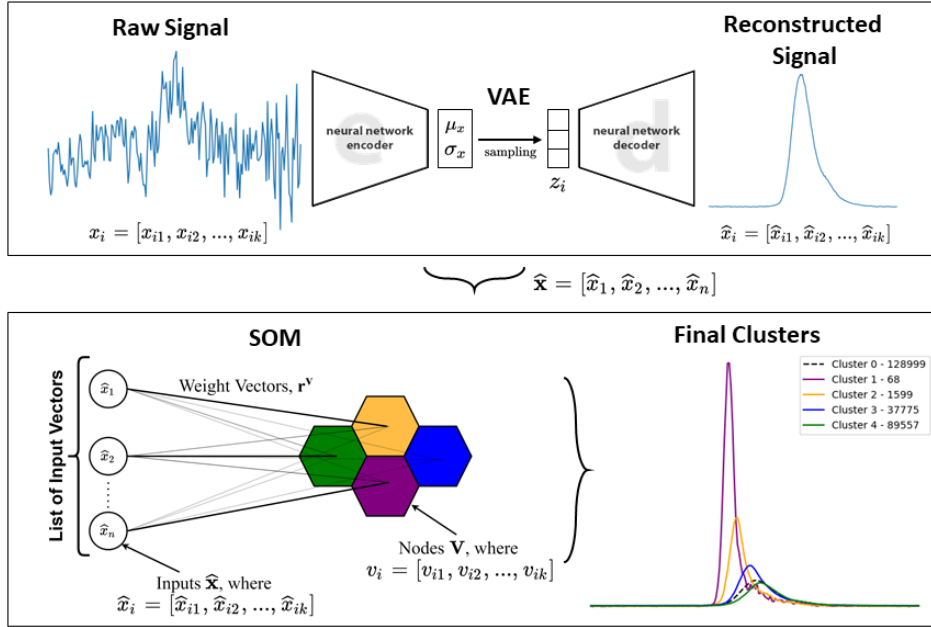


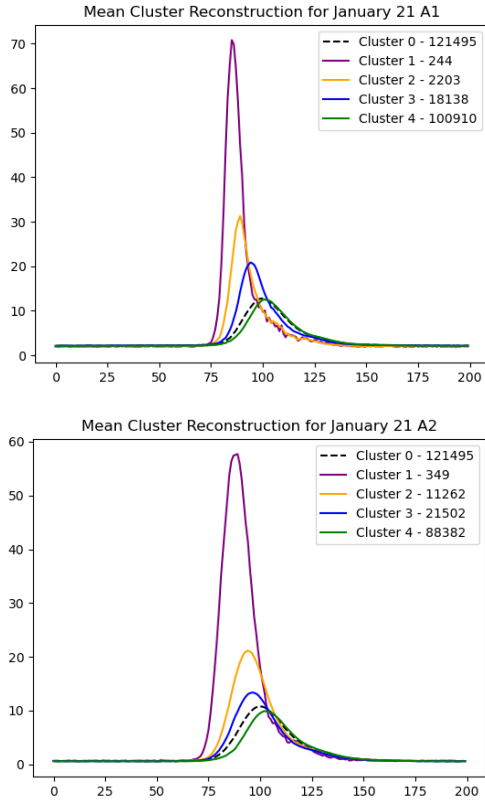
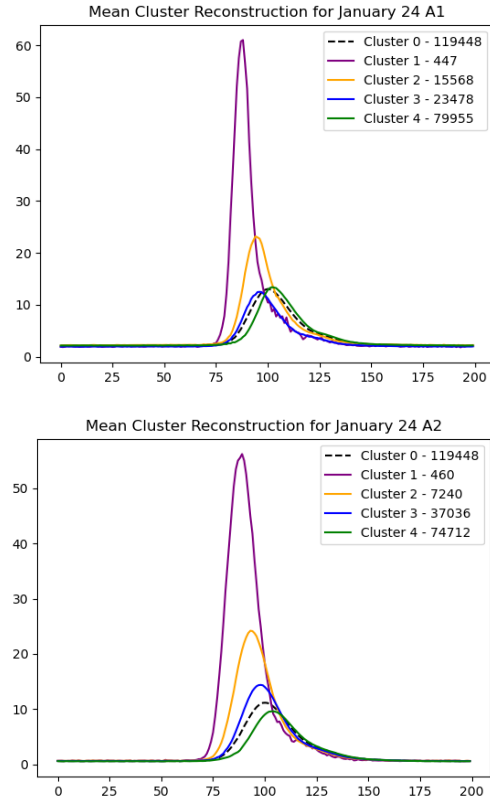
Figure 11. Schematics of the VAE reconstruction of all N individual pulses signals and of SOM clustering.

Table 4. SOM Clustering for 2021-01-24 with Antennas 1 and 2.

	Cluster #	0	1	2	3	4
A1	# pulses	119448	447	15568	23478	79955
	peak loc	99.77 ± 5.64	86.46 ± 2.26	93.25 ± 3.51	94.62 ± 3.52	102.63 ± 4.03
	peak height	17.03 ± 11.10	86.96 ± 50.04	29.56 ± 17.44	13.96 ± 4.21	15.09 ± 6.41
	peak width	17.39 ± 4.32	6.07 ± 1.14	10.84 ± 3.23	17.33 ± 3.64	18.43 ± 3.77
	peak skew	2.50 ± 0.43	4.55 ± 0.58	3.07 ± 0.48	2.47 ± 0.27	2.38 ± 0.32
	Cluster #	0	1	2	3	4
A2	# pulses	119448	460	7240	37036	74712
	peak loc	100.53 ± 4.80	88.15 ± 2.62	92.90 ± 2.91	96.91 ± 3.08	103.14 ± 3.38
	peak height	12.93 ± 6.67	62.24 ± 24.60	26.32 ± 8.78	15.25 ± 3.98	10.17 ± 3.07
	peak width	21.92 ± 1.99	14.76 ± 0.56	17.22 ± 0.93	21.61 ± 1.50	22.73 ± 1.36
	peak skew	2.11 ± 0.22	2.95 ± 0.11	2.52 ± 0.13	2.22 ± 0.13	2.01 ± 0.18

Table 5. SOM Clustering for 2021-01-28 with Antennas 1 and 2. This set was used for A1 and A2 VAE training.

	Cluster #	0	1	2	3	4
A1	# pulses	128999	68	1599	37775	89557
	peak loc	99.52 ± 5.82	83.57 ± 1.47	87.21 ± 2.24	95.19 ± 3.90	101.57 ± 5.22
	peak height	17.94 ± 12.39	132.11 ± 46.02	53.42 ± 39.95	25.15 ± 14.62	14.18 ± 5.70
	peak width	17.27 ± 4.54	5.72 ± 0.61	6.98 ± 1.91	12.52 ± 3.54	18.85 ± 3.79
	peak skew	2.54 ± 0.44	5.06 ± 0.41	3.91 ± 0.65	2.87 ± 0.42	2.38 ± 0.30
A2	Cluster #	0	1	2	3	4
	# pulses	128999	117	2344	25574	100964
	peak loc	100.45 ± 5.04	85.74 ± 2.53	89.95 ± 2.37	94.85 ± 2.95	102.13 ± 4.07
	peak height	15.64 ± 8.54	104.39 ± 24.05	44.33 ± 18.04	22.83 ± 7.61	13.05 ± 4.71
	peak width	21.81 ± 2.62	14.08 ± 0.59	15.71 ± 0.74	17.97 ± 0.99	22.64 ± 2.21
peak skew	2.20 ± 0.23	3.12 ± 0.08	2.79 ± 0.12	2.43 ± 0.14	2.13 ± 0.19	

**Figure 12.** Distribution of the SOM clustering average signals for the observations 2021-01-21. Radio telescope A1 on top and Radio telescope A2 on bottom with respective VAE training performed on the January 28 observation.**Figure 13.** Distribution of the SOM clustering average signals for the observations 2021-01-24. Radio telescope A1 on top and Radio telescope A2 on bottom with respective VAE training performed on the January 28 observation.

naturally appears with negative heights with respect to the average pulse location since it has to compensate the positive contributions of the larger amplitude clusters. The shift is relatively small since cluster 4 is the overwhelming most numerous cluster, except of the special configuration of A1 during March 29th observation.

The location of the four components seems to roughly follow those studied in [Krishnamohan & Downs \(1983\)](#) (See their Fig. 16), with distances between components ranging from 100 km to 500 km. The coincidence on the scale of distances is perhaps expected from the decomposition of the main pulse into ordered components (See Fig. 9 in [Krishnamohan & Downs \(1983\)](#)). Further studies of the Vela radio emission region [Gwinn et al. \(1997\)](#) also estimate its size in about

Table 6. Magnetosphere altitude in kilometers for each of the pulse clusters presented in Sec. 3.3.

	Cluster	1	2	3	4
A1	Jan 21	313.7 ± 41.5	253.1 ± 47.2	131.7 ± 68.7	-29.9 ± 110.9
	Jan 24	292.2 ± 49.6	143.1 ± 77.1	113.1 ± 77.3	-62.8 ± 88.5
	Jan 28	350.1 ± 32.3	270.2 ± 49.2	95.1 ± 85.6	-45.0 ± 114.6
	Mar 29	306.0 ± 57.7	108.9 ± 83.0	104.7 ± 108.0	-92.6 ± 95.1
A2	Jan 21	275.7 ± 62.3	148.4 ± 71.3	110.0 ± 61.0	-46.8 ± 74.2
	Jan 24	271.8 ± 57.5	167.5 ± 63.9	79.5 ± 67.6	-57.3 ± 74.2
	Jan 28	322.9 ± 55.5	230.5 ± 52.0	122.9 ± 64.8	-36.9 ± 89.3
	Mar 29	345.3 ± 57.3	261.2 ± 53.8	137.4 ± 75.3	-33.8 ± 99.4

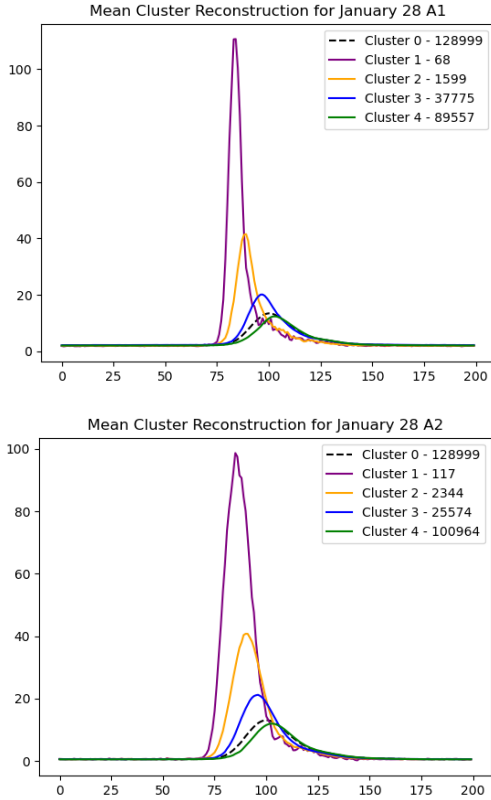


Figure 14. Distribution of the SOM clustering average signals for the observations 2021-01-28. Radio telescope A1 on top and Radio telescope A2 on bottom. VAE training has been performed on these observations.

500 km from the modulation of the pulsar’s scintillation. While more recent and detailed studies [Gwinn et al. \(2012\)](#) of the scintillation properties at 18 cm wavelength describe the early part of the pulse from -400 km to the later part of the pulse to $+800$ km with respect to its peak. While using novel scintillation statistics techniques at 760 MHz [Johnson et al. \(2012\)](#) find that the radio emission altitude for the Vela pulsar is less than 340 km.

4 CONCLUSIONS

In this paper we have performed a prototypical study of individual pulses of Vela using standard machine learning techniques. We have assumed an agnostic approach to the data and applied clustering DBSCAN and SOM techniques independently to analyze the top amplitude pulses and a global dissection of the pulses respectively. The former provided us with a way to stratify those mini-giant pulses that are relatively rare but still appear in each day of observation. The SOM techniques are applied after a VAE reconstruction of the pulses with a training on the best day of observation (based on a S/N criteria). We have found a robustness of the clustering this way over the days of observations and antennas, which represents an important cross-check of our systematics.

The simple statistical distribution of the pulse amplitudes was found to be roughly fitted by the scintillation function (1) (a χ^2 -distribution) and we have been able to provide effective n_{ISS} indices with rather high values, ranging from around 7 to 10. While this fit

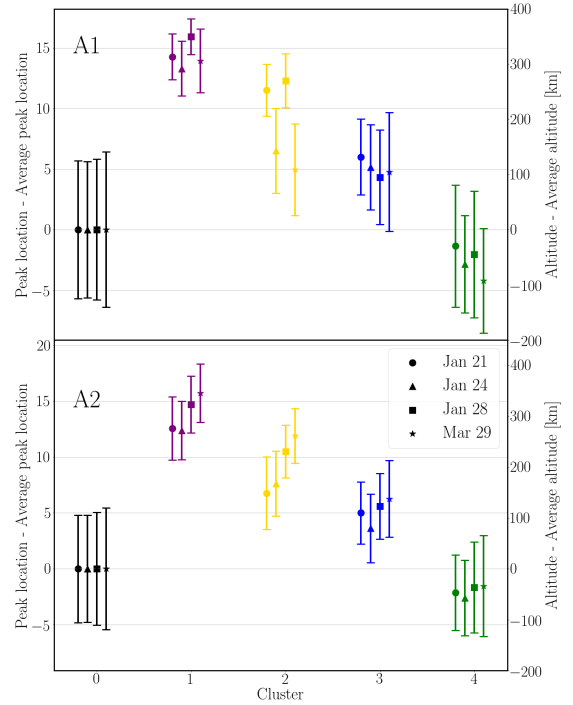


Figure 15. Peak location and magnetosphere altitude, with the corresponding error bars, for each of the pulse clusters presented in Sec. 3.3.

is rather good (See Fig. 9) it leaves a residual high amplitude set of pulses that cannot be simply explained by scintillation, suggesting there is an intrinsic pulsar emission of those mini-giant pulses. We couple this to the observation of those pulses arriving earlier than the average pulse during the over 3 hours of our daily observations (See Figs. 3,5,7) to support a simple model based on the height location of the emission regions in the pulsar magnetosphere for those large amplitude pulses. We use the SOM clustering to determine four relevant sets of pulses characteristics that seem to linearly array along the emission regions of the magnetosphere (See Fig. 15) separated by roughly 100km each. Those results, based on Machine learning clustering, seem to agree with specific studies of the Vela pulses and its scintillation responses.

This first study provides us with a proof-of-principle technique to be applied more massively to daily observations of Vela. Our studies for the distribution of pulses amplitudes, widths and peaks timing have been performed in a relatively calm period of Vela, in between major glitches. Of particular interest is to study if any of these properties suffers a change or provides precursor information of the mayor glitches Vela suffers every 2–3 years. The most recent one took place on July 21st 2021 [Sosa-Fiscella et al. \(2021b\)](#) (while this paper was nearing completion) and the previous one was on February 1st, 2019 (See [Gancio et al. \(2020\)](#) and references there in).

The fact that high amplitude pulses are also thinner, could have implications for their use for pulsar timing [Kerr \(2015\)](#). In particular, if this features is also carried out to millisecond pulsars, like PSR J0437–4715, this can further improve its timing to detect grav-

itational waves from supermassive binary black holes [Sosa Fiscella et al. \(2021a\)](#) and will be the subject of study of a forthcoming paper. Another pulsar of interest for single pulses study in the southern hemisphere that is being observed at IAR is PSR B1641–45/J1644–4559 [Johnston \(2004\)](#).

ACKNOWLEDGEMENTS

We thank Yogesh Maan for numerous beneficial discussions about the best use of RFIClean, Cameron Knight and Carolina Negrelli for participating in the early studies involving machine learning techniques, and Adolfo Simaz Bunzel and Ezequiel Zubieta in the observations reduction pipeline. COL gratefully acknowledge the National Science Foundation (NSF) for financial support from Grants No. PHY-1912632 and PHY-2018420. JAC and FG acknowledge support by PIP 0102 (CONICET). JAC is CONICET researcher. This work received financial support from PICT-2017-2865 (AN-PCyT). JAC was also supported by grant PID2019-105510GB-C32/AEI/10.13039/501100011033 from the Agencia Estatal de Investigación of the Spanish Ministerio de Ciencia, Innovación y Universidades, and by Consejería de Economía, Innovación, Ciencia y Empleo of Junta de Andalucía as research group FQM-322, as well as FEDER funds.

DATA AVAILABILITY

Data generated by our calculations or observations are available from the corresponding authors upon reasonable request.

REFERENCES

Agarwal D., Aggarwal K., Burke-Spolaor S., Lorimer D. R., Garver-Daniels N., 2020, *MNRAS*, **497**, 1661

Andersson N., Glampedakis K., Ho W. C. G., Espinoza C. M., 2012, *Phys. Rev. Lett.*, **109**, 241103

Ankerst M., Breunig M. M., Kriegel H.-P., Sander J., 1999, in Proc. ACM SIGMOD Int. Conf. on Management of Data (SIGMOD'99). Philadelphia, PA, pp 49–60

Astropy Collaboration et al., 2013, *A&A*, **558**, A33

Astropy Collaboration et al., 2018, *AJ*, **156**, 123

Bethapudi S., Desai S., 2018, *Astronomy and Computing*, **23**, 15

Cairns I. H., Johnston S., Das P., 2001, *ApJ*, **563**, L65

Chamel N., 2013, *Phys. Rev. Lett.*, **110**, 011101

Cordes J. M., 2000, arXiv e-prints, pp astro-ph/0007233

Cordes J. M., Chernoff D. F., 1997, *ApJ*, **482**, 971

Cordes J. M., Downs G. S., Krause-Polstorff J., 1988, *ApJ*, **330**, 847

Devine T. R., Goseva-Popstojanova K., McLaughlin M., 2016, *MNRAS*, **459**, 1519

Dodson R., Lewis D., McCulloch P., 2007, *Astrophysics and Space Science*, **308**, 585

Eatough R. P., Keane E. F., Lyne A. G., 2009, *MNRAS*, **395**, 410

Ester M., Kriegel H.-P., Sander J., Xu X., 1996, in Proc. of 2nd International Conference on Knowledge Discovery and. pp 226–231

Gancio G., et al., 2020, *A&A*, **633**, A84

Gold T., 1968, Rotating Neutron Stars as the Origin of the Pulsating Radio Sources. Springer US, Boston, MA, pp 74–75, doi:10.1007/978-1-4899-6387-1_40, https://doi.org/10.1007/978-1-4899-6387-1_40

Goldreich P., Julian W. H., 1969, *ApJ*, **157**, 869

Guo P., et al., 2019, *MNRAS*, **490**, 5424

Gwinn C. R., et al., 1997, *ApJ*, **483**, L53

Gwinn C. R., et al., 2012, *ApJ*, **758**, 7

Gyawali P., Li Z., Knight C., Ghimire S., Horacek B. M., Sapp J., Wang L., 2019, in 2019 IEEE International Conference on Data Mining (ICDM). pp 1078–1083

Haskell B., Melatos A., 2015, *International Journal of Modern Physics D*, **24**, 1530008

Hewish A., Bell S. J., Pilkington J. D. H., Scott P. F., Collins R. A., 1968, *Nature*, **217**, 709

Johnson M. D., Gwinn C. R., Demorest P., 2012, *ApJ*, **758**, 8

Johnston S., 2004, *MNRAS*, **348**, 1229

Johnston S., van Straten W., Kramer M., Bailes M., 2001, *The Astrophysical Journal*, **549**, L101

Kerr M., 2015, *MNRAS*, **452**, 607

Kingma D. P., Welling M., 2014, Auto-Encoding Variational Bayes ([arXiv:1312.6114](https://arxiv.org/abs/1312.6114))

Knuth K. H., 2006, arXiv e-prints, p. physics/0605197

Kohonen T., 1988, Self-Organized Formation of Topologically Correct Feature Maps. MIT Press, Cambridge, MA, USA, p. 509–521

Kramer M., Johnston S., van Straten W., 2002, *Mon. Not. Roy. Astron. Soc.*, **334**, 523

Krishnamohan S., Downs G. S., 1983, *ApJ*, **265**, 372

Lam M. T., 2017, PyPulse: PSRFITS handler (ascl:1706.011)

Large M. I., Vaughan A. E., Mills B. Y., 1968, *Nature*, **220**, 340

LeCun Y., Bengio Y., Hinton G., 2015, *nature*, **521**, 436

Lin H., Li X., Luo Z., 2020, *MNRAS*, **493**, 1842

Lopez Armengol F. G., et al., 2019, The Astronomer's Telegram, **12482**, 1

Lorimer D. R., 2008, *Living Reviews in Relativity*, **11**, 8

Lorimer D. R., Kramer M., 2012, Handbook of Pulsar Astronomy. Cambridge University Press

Maan Y., van Leeuwen J., Vohl D., 2021, *A&A*, **650**, A80

Mateos D. M., Riveaud L. E., Lamberti P. W., 2017, *Chaos*, **27**, 083118

Michilli D., et al., 2018, *MNRAS*, **480**, 3457

Morello V., Barr E. D., Bailes M., Flynn C. M., Keane E. F., van Straten W., 2014, *MNRAS*, **443**, 1651

Morello V., et al., 2019, *MNRAS*, **483**, 3673

Pacini F., 1967, *Nature*, **216**, 567

Palfreyman J., Dickey J. M., Hotan A., Ellingsen S., van Straten W., 2018, *Nature*, **556**, 219

Pang D., Goseva-Popstojanova K., Devine T., McLaughlin M., 2018, *MNRAS*, **480**, 3302

Piekarewicz J., Fattoyev F. J., Horowitz C. J., 2014, *Phys. Rev. C*, **90**, 015803

Radhakrishnan V., Cooke D. J., 1969, *Astrophys. Lett.*, **3**, 225

Radhakrishnan V., Manchester R. N., 1969, *Nature*, **222**, 228

Radhakrishnan V., Cooke D. J., Komesaroff M. M., Morris D., 1969, *Nature*, **221**, 443

Ransom S., 2018, PRESTO - Pulsar Exploration and Search Toolkit, <https://www.cv.nrao.edu/~sransom/presto/>

Reichley P. E., Downs G. S., 1969, *Nature*, **222**, 229

Sarkissian J., Hobbs G., Reynolds J., Palfreyman J., Olney S., 2019, The Astronomer's Telegram, **12466**, 1

Schubert E., Sander J., Ester M., Kriegel H., Xu X., 2017, *ACM Transactions on Database Systems*, **42**, 1

Shu R., 2014, Gaussian Mixture VAE: Lessons in Variational Inference, Generative Models, and Deep Nets., <http://ruishu.io/2016/12/25/gmvae/>

Sosa Fiscella V., et al., 2021a, *Astrophys. J.*, **908**, 158

Sosa-Fiscella V., et al., 2021b, The Astronomer's Telegram, **14806**, 1

Sturrock P. A., 1971, *ApJ*, **164**, 529

Van der Maaten L., Hinton G., 2008, Journal of machine learning research, **9**

Wang H., et al., 2019, *Science China Physics, Mechanics, and Astronomy*, **62**, 959507

Zhang Y. G., Gajjar V., Foster G., Siemion A., Cordes J., Law C., Wang Y., 2018, *ApJ*, **866**, 149

Zhang C., et al., 2020, *A&A*, **642**, A26

Zhu W. W., et al., 2014, *ApJ*, **781**, 117

APPENDIX A: SINGLE PULSES EXTRACTION

While conventional timing techniques involve folding observations in time and frequency to obtain an integrated pulse profile, for our purposes of performing single-pulse analysis we have devised an algorithm to extract the single pulses:

- (i) For starters, each observation is folded using the `prepfold` routine from the pulsar search and analysis software PRESTO (Ransom 2018). As a byproduct, the pulsar period along the observation is modeled as a polynomial function in time, and the corresponding coefficients are saved to a `polycos` file that we save for later use.
- (ii) We de-disperse and integrate our data in frequency. We use a script adapted from `waterfall.py` in the PRESTO package (Ransom 2018). For the dispersion measure, we use the value 67.897/68.053 for the January observations with A1/A2, and 68.057 for the March observations with A1 or A2. After this step, the observation is reduced to a single array in time.
- (iii) We proceed to build a grid in time where each instantaneous period of the pulsar is divided by a fixed number of time bins. In this way, we account for the intrinsic pulsar spin-down during the observation, and the single pulses will arrive approximately at the same phase. We use the file `polycos` to calculate the period for each single pulse, and divided that period into a fixed number of time bins. We use 1220 bins per period, approximated by dividing an average period of Vela by our time resolution $89.2\text{ms}/73\mu\text{s} \approx 1220$.
- (iv) The original observational data was sampled at time intervals that do not necessarily match our time grid. We therefore interpolated the datum that would correspond to each mesh point from the data in the adjacent actual measured points.
- (v) We applied this process to observations taken with each of the radio telescopes, and that overlapped for at least 3 hours.
- (vi) In order to obtain truly simultaneous observations, we cropped the interpolated data to obtain two observations that start and finish at the same MJDs.

The resulting `.fil` files thereby obtained are then cleansed of RFIs using the algorithms described in Appendix C.

APPENDIX B: OTHER ANALYSIS METHODS

Besides standard isotropic Gaussian as priors for the latent representation of vela pulse, we explored non-parametric alternatives via Indian Buffet Process (IBP) as prior in VAE (Gyawali et al. 2019). With IBP, we aimed to cluster the latent representation into multiple factors in an unsupervised way. However, in this study, we find standard Gaussian prior to work better.

Additionally, we tried to apply the Gaussian Mixture VAE (GM-VAE) in (Shu 2014). We found that the Gaussian mixture consistently collapsed into one or two super-clusters and failed to give meaningful results.

Outside of the SOM, another clustering method tried was Agglomerative Clustering (based on the SciPy implementation <https://scikit-learn.org/stable/modules/clustering.html#hierarchical-clustering>) where observations are continually merged together into larger groupings based on linkage criterion. We found that this produced decent clusters on small datasets, however found that it was computationally prohibitive to apply on increasingly larger sets.

A t-distributed stochastic neighbor embedding (t-SNE) algorithm in (Van der Maaten & Hinton 2008) was applied on the raw data to see if clusters could be found in an embedded space outside of

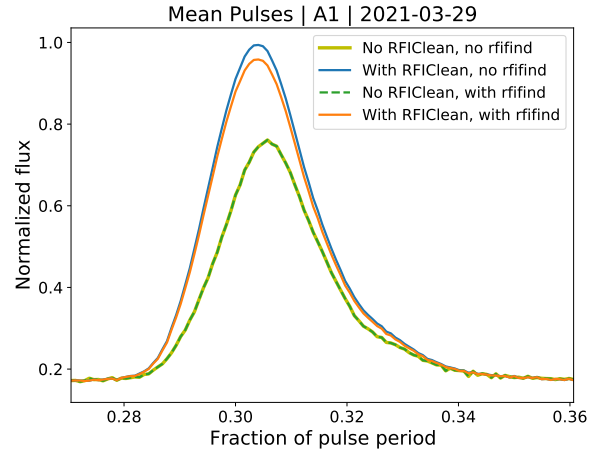


Figure C1. Mean pulses for the March 29th observation using four different RFI-cleaning schemes. The fluxes are uncalibrated and are in arbitrary units.

deep learning. While organization of signals were observed in this 2-dimensional space, it was primarily a result on when the spike happened in the signal. We observed the same computational issues with this method when extending to the larger datasets.

APPENDIX C: CLEANING OF RADIO FREQUENCY INTERFERENCE

Time de-dispersion with unfiltered radio frequency interferences (RFIs) results in a modulation of the signal. Therefore, the RFIs must be filtered from the raw data before extracting single pulses. In this work we tested two complementary RFI-cleaning softwares:

- `rfind` is a task within PRESTO (Ransom 2018) that searches for narrow-band and short duration broadband RFI by identifying outliers using time domain statistics (mean and standard deviation of each time bloc). Flagged blocks are replaced in subsequent processing by constant data that is chosen based on the median bandpass.
- RFIClean (Maan et al. 2021) removes *periodic* RFI in each individual frequency channel using Fourier domain analysis. After that, it uses threshold-based techniques to identify time samples as well as frequency channels contaminated by broadband bursts and narrow-band RFI. The identified samples are replaced by mean values in the local regions around the affected samples.

Periodic RFI could limit the efficacy of conventional RFI mitigation techniques used by `rfind`, since they could potentially result in masking a large fraction of the data. Consequently, we assess the benefits of incorporating RFIClean into our RFI cleaning schemes.

We found that RFIClean gave better results both at mitigating RFIs and providing a higher mean pulse amplitude, as evidenced in Fig. C1. The S/N ratios attained using each cleaning algorithm are presented in Table C1. We can readily see that:

- (i) The A1 observations are more heavily affected by RFIs, as evidenced when no RFI cleaning scheme is applied. They also benefit more from using RFIClean than `rfind`.
- (ii) A2 observations do not present a preference for any cleaning algorithm. Moreover, an over-masking occurs in the January 24th observations when using only one of them.

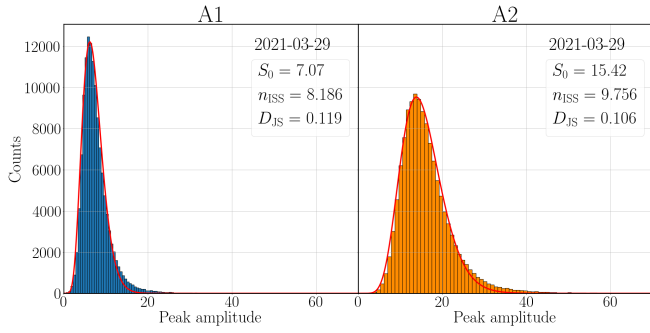


Figure D1. Histograms of projected pulse amplitude for J0835–4510 for A1 (left) and A2 (right) for the 2021-03-29 observation. The line shows the estimated scintillation distribution from fitting n_{ISS} in Eq. (1).

(iii) The quality of the March observations with A1 is severely hindered, possibly due to the different observational setting used in those (two polarizations modes instead of one).

(iv) Overall, we see an improvement in S/N when using either RFI mitigation technique. Moreover, we found that using `rfifind` on the data output from `RFIClean` further improves the S/N in many cases, as predicted by [Maan et al. \(2021\)](#).

We therefore ran both programs in all observations. To avoid a possible modification of the periodic signal, we set `RFIClean` to safeguard the Fourier frequency corresponding to the pulsar’s spin period (via the `-psrf <F0>` modifier). Moreover, given Vela’s relatively long spin period, we provided a block size large enough to cover at least 100 of pulsar periods (via `-t`). Otherwise, if the specified block size is not sufficiently long enough, `RFIClean` is unable to detect the corresponding spin frequency in the Fourier domain. Including the `-zerodm` modifier (useful for searching for unknown periodic or transient signals) resulted in a pulse distortion, as noted by [Eatough et al. \(2009\)](#), and this option was thereby avoided.

APPENDIX D: OBSERVATIONS 2021-03-29

In this section we perform a simultaneous observation with a different A1 configuration. We have chosen to observe in a two polarization, 56MHz+56MHz mode, to mimic more closely the observation mode of A2 and further compare the results of the two radio telescopes as an ultimate cross-check.

D1 Scintillation for 2021-03-29

As described in Sec. 3.2, we also fitted Eq. (1) to the pulse amplitude distribution of the March 29th dataset. In this case, we see that the A1 distribution is tilted towards lower amplitudes, while the A2 distribution is consistent with the previous datasets. We thereby conclude that the A1 observation suffers from a quality loss, possibly due to a malfunction in one of the two polarization modes that were used in this configuration. However, the fitted values of n_{ISS} for the A2 observation are in good agreement with the corresponding results in Table 2. Therefore, these results are not particular to the January observations but rather part of a more general behaviour when analyzing short timescale scintillation.

D2 Observations 2021-03-29 with DBSCAN analysis

Fig. D2 displays on the left column the distribution of the pulses amplitudes versus arrival time as measured by the position of their peaks. Insets show the histograms of pulse amplitudes for each observation. We observe again, that there is a trend for peaks with larger amplitudes to appear earlier than pulses with lower amplitude indicating this is a generic feature. We also note now the similarity of the patterns of A1 and A2 observations with A1 now configured into two polarizations, like A2. On the right column, Fig. D2 displays the distribution of the pulses amplitudes versus its mean width as measured by the half amplitude of their peaks. There is a very weak trend, if at all, for peaks with larger amplitudes to appear narrower than pulses with lower amplitude in Radio telescope A1 observations in this new configuration. This is confirmed by the corresponding observation with Radio telescope A2, suggesting a dependence of this effect on the single polarization observations with A1 during the January runs.

We next performed a Density Based Scan (DBSCAN) analysis of the pulses clustering for each Radio telescope’s observation as displayed in Fig. D3 which selects the different clusters by increasing amplitudes, but also creates a baseline cluster (in orange labeled as 0) and an enveloping outlier (in light blue, labeled as -1). We also display the detail of each pulse in the top amplitude DBSCAN clusters over the duration of the observation, labeled by the pulse index number. It is interesting to see here no particular preference of the large amplitude pulses toward a time of the duration of the observation, indicating that during this March observation there seems not to be a preferential direction of the local RFIs.

D3 Observations 2021-03-29 with VAE/SOM analysis

In Fig. D4 we display the average value of the pulses in each SOM cluster for each Radio telescope observation. Those have been obtained by first applying a reconstruction of the raw pulses with the VAE technique, for which we have used the reconstruction of our best day of observation (according to the analysis in Appendix C) as a training case to apply to the rest of the days of observation. This training has been applied for each antenna individually. SOM allows us to specify then the number of clusters we seek to subdivide the whole set. We have studied several possible cases, 4, 6, 10, 25, 100, finding that the simplest four cluster choice represents the most robust results. We observe in Fig. D4 the degradation of the A1 observation while we also see the similarity of the mean clustering between the A2 and the two antennas previous observations. While the total number of members of each cluster changes, the qualitative mean value of the pulses (average pulse over the entire cluster) seems to be robust. We also note the visual displacement towards earlier times of the center and peak of each cluster average pulse for those with the largest amplitude with respect to each other and with respect to the total average pulse, in the plot denoted by the black dashed curve and labeled as 0. This is the usual reference pulse we obtain from the total observation. We also see that the largest amplitude cluster (labeled as 1), counting a few hundred pulses, is a factor about 7 larger in amplitude than the average pulse. Both features are in qualitative agreement with the statistical analysis of the previous section 3.1.

Table D1 give a quantitative account of the results displayed in Fig. D4. For each antenna’s observation on 2021-03-29, we provide the number of pulses of each cluster # pulses; peak location from the index of the maximum value in the pulse sequence; peak height from the maximum value of the pulse sequence; peak width done by first finding the maximum value of the sequence, then performing full-width half maximum of peak; (library used

Table C1. S/N for each observation and each RFI cleaning scheme. These values were obtained using the `sp.getSN()` class attribute from the `PyPulse` package (Lam 2017).

	No RFIclean		No RFIclean		RFIclean		RFIclean	
	No rfind		rfind		No rfind		rfind	
	A1	A2	A1	A2	A1	A2	A1	A2
Jan21	429.41	2084.61	1936.58	1967.86	1982.96	2038.37	2100.66	2107.03
Jan24	1145.38	2108.17	1894.91	2182.69	1983.3	2142.97	2005.07	2188.26
Jan28	529.90	2575.20	2163.26	2714.59	2188.04	2676.22	2193.6	2746.39
Mar29(*)	661.08	2062.26	1010.64	2121.49	1125.62	2192.01	1115.69	2192.23

(*) **Note.** March 29th observation with A1 used a different configuration with two polarizations.

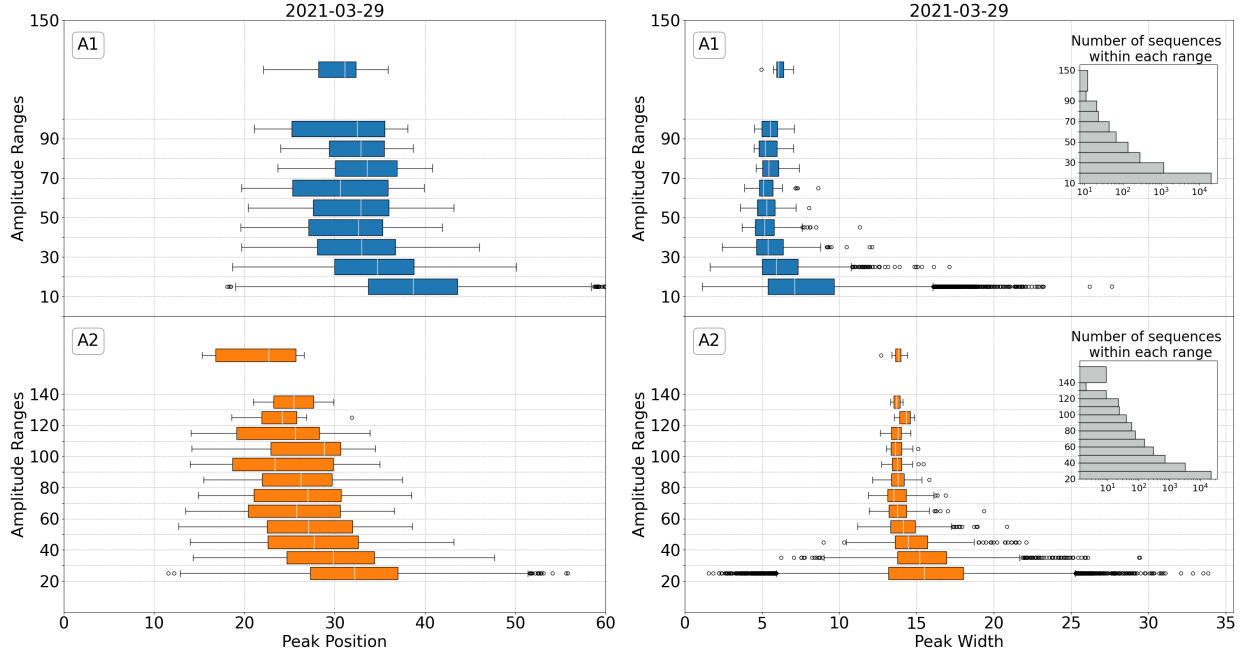


Figure D2. Distribution of the pulses amplitudes versus arrival time as measured by the position of their peaks for the 2021-03-29 observations and distribution of the pulses amplitudes versus its mean widths for the Radio telescope A1 on top and Radio telescope A2 on bottom. The differences in behavior can be attributed to the single polarization versus two polarizations observations with A1 and A2 respectively.

for this: https://docs.scipy.org/doc/scipy/reference/generated/scipy.signal.peak_widths.html); for the peak skew we evaluated the Fisher-Pearson coefficient of skewness; (using the scipy for this computation <https://docs.scipy.org/doc/scipy/reference/generated/scipy.stats.skew.html>); and finally MSE is the standard mean squared error. $\sum_{i=1}^N (x_i - \bar{x})^2 / N$. The trend in the peak location towards later times is clear and above the quoted errors in its determination. Note that the cluster 4, the most numerous, is (necessarily) showing a later arrival than the average total pulse, labeled as 0. A trend is also marginally seen in the width of the pulse, with narrower values for the higher amplitude clusters while also carrying a higher skewness. Although specific numbers differ in both antennas observations, the trends seem to be the same, including the particular case of the A1 configuration during this observation.

This paper has been typeset from a $\text{\TeX}/\text{\LaTeX}$ file prepared by the author.

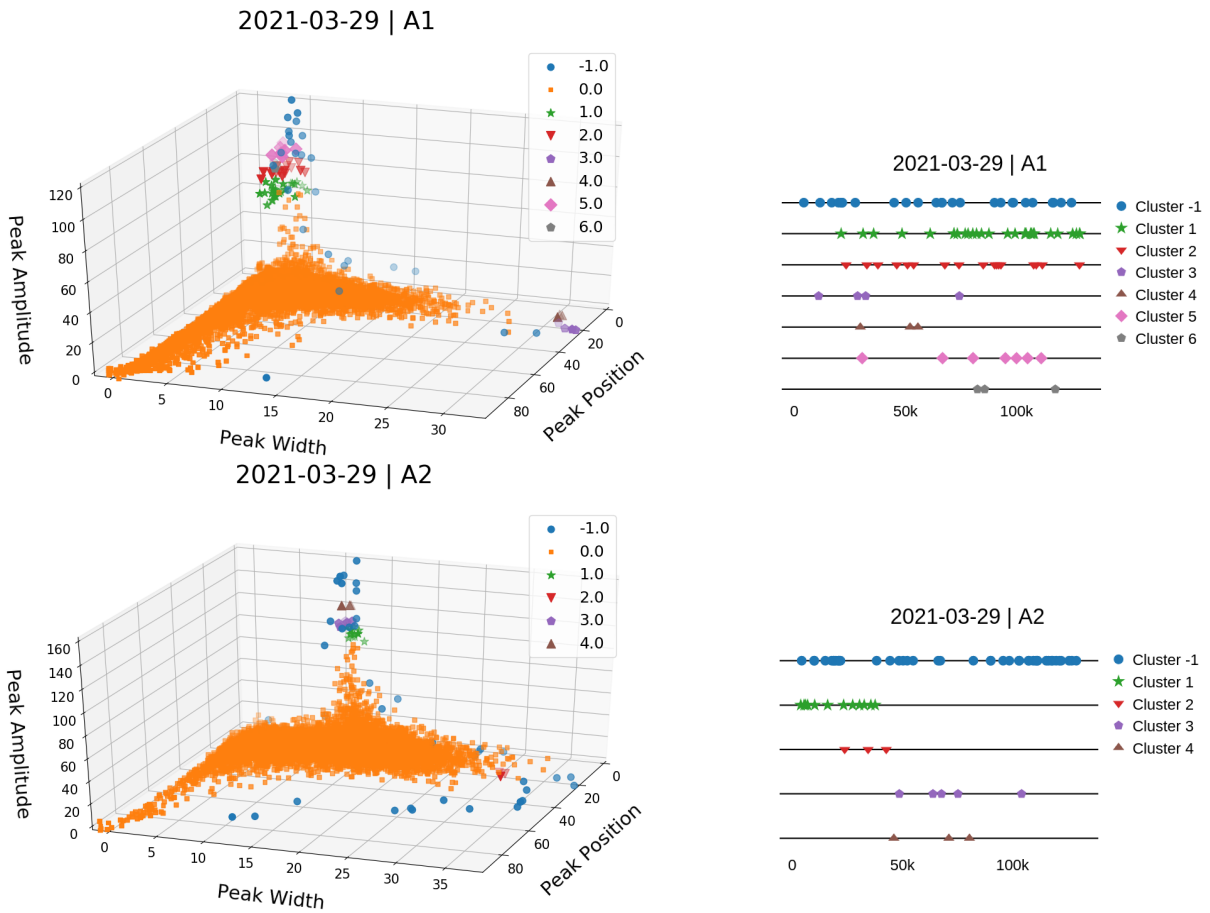


Figure D3. (On the left) 3D distribution of the pulses peak amplitudes, position, and widths for the 2021-03-29 observations. Radio telescope A1 on top and Radio telescope A2 on bottom. Different colors represent different clusters according to density based scan criteria. (On the right) Distribution of the pulses over the duration of the observations 2021-03-29. Upper figures as for Radio telescope A1, lower figures are for Radio telescope A2 on. Different colors represent different clusters according to density based scan criteria.

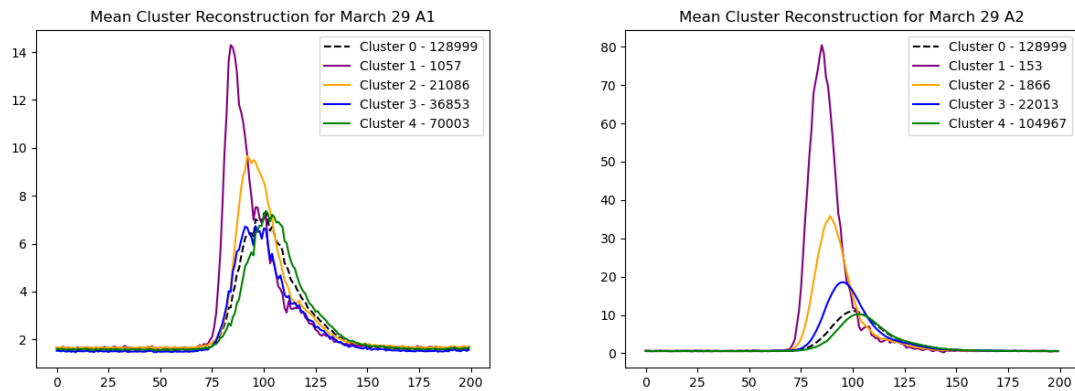


Figure D4. Distribution of the SOM clustering average signals for the observations 2021-03-29. Radio telescope A1 on left and Radio telescope A2 on right panels, with respective VAE training performed on the January 28 observation. Note that A1 was changed to two-polarizations configuration here.

Table D1. SOM Clustering for 2021-03-29 with Antennas 1 and 2. A1 configuration has been changed here to two polarizations mode.

	Cluster #	0	1	2	3	4
A1	# pulses	128999	1057	21086	36853	70003
	peak loc	98.72 ± 6.42	84.78 ± 2.63	93.76 ± 3.78	93.95 ± 4.92	102.94 ± 4.33
	peak height	8.46 ± 2.97	17.76 ± 13.30	10.99 ± 4.68	7.45 ± 0.97	8.09 ± 1.59
	peak width	21.51 ± 4.34	11.04 ± 4.98	18.88 ± 3.52	19.41 ± 4.36	22.43 ± 4.00
	peak skew	2.06 ± 0.29	2.83 ± 0.70	2.38 ± 0.28	2.00 ± 0.21	1.99 ± 0.22
	MSE	0.00005 ± 0.00009	0.00781 ± 0.02791	0.00034 ± 0.00067	0.00016 ± 0.00027	0.00009 ± 0.00015
	Cluster #	0	1	2	3	4
A2	# pulses	128999	153	1866	22013	104967
	peak loc	100.49 ± 5.46	84.76 ± 2.61	88.59 ± 2.45	94.23 ± 3.43	102.03 ± 4.53
	peak height	13.31 ± 7.12	86.35 ± 27.48	38.66 ± 14.61	20.43 ± 6.75	11.27 ± 3.71
	peak width	19.54 ± 1.54	13.91 ± 0.98	15.58 ± 0.77	19.41 ± 1.30	21.93 ± 1.32
	peak skew	2.12 ± 0.23	3.14 ± 0.11	2.76 ± 0.13	2.38 ± 0.13	2.06 ± 0.19
	MSE	0.00009 ± 0.00013	0.10855 ± 0.26202	0.00676 ± 0.01160	0.00052 ± 0.00080	0.00011 ± 0.00016